Titania photonic crystal photocatalysts functionalized by graphene oxide nanocolloids

Angeliki Diamantopoulou[a], Elias Sakellis[b], George Em. Romanos[b], Spyros Gardelis[a], Nikolaos Ioannidis[b], Nikolaos Boukos[b], Polycarpos Falaras[b,*], Vlassis Likodimos[a,*]

[a] *Section of Solid State Physics, Department of Physics, National and Kapodistrian University of Athens, Panepistimiopolis, 15 784, Greece*
[b] *Institute of Nanoscience and Nanotechnology, National Center for Scientific Research "Demokritos", 15341 Agia Paraskevi, Athens, Greece*

ARTICLE INFO

ABSTRACT

Photonic crystal-assisted semiconductor photocatalysis has been attracting significant attention as an advanced photon management approach that combines light harvesting with the macro/mesoporous structured materials properties permitting enhanced mass transport and high adsorption. In this work, surface functionalization of well-ordered photonic band gap engineered TiO_2 inverse opal films fabricated by the convective evaporation-induced co-assembly method was performed by graphene oxide nanocolloids (nanoGO). The loading of GO nanosheets was determined by the films' macropore size, with minimal effects on their long range periodicity and photonic properties. While nanoGO deposition reduced mesoporosity of the nanocrystalline titania walls, their surface functionality was greatly improved by the abundant oxygen groups of the GO nanosheets leading to increased pollutant adsorption. Slow photon amplification in the aqueous phase methylene blue photo-degradation was identified for the unmodified TiO_2 photonic films under both UV–vis and Vis illumination upon spectral overlap of the low energy edge of the inverse opal stop band (in water) with the dye electronic absorption, due to (red) slow photons localized in the titania skeleton that distinctly accelerated dye photo-degradation kinetics. The photocatalytic efficiency was further improved for the nanoGO functionalized TiO_2 inverse opal films via the synergetic action of interfacial electron transfer from TiO_2 to the GO nanosheets. Under UV–vis light, the functionalized photonic films outperformed benchmark mesoporous Aeroxide® P25 TiO_2 films where nanoGO modification, despite the enhanced dye adsorption, resulted in adverse effects in photocatalytic degradation due to pore clogging. Combination of the exceptional structural and photonic properties of TiO_2 inverse opals with the high adsorption capacity and charge separation afforded by GO nanocolloids is proposed as a promising modification route for the development of efficient photocatalytic films.

1. Introduction

Titanium dioxide (TiO_2) photocatalysis has been established as an advanced oxidation/reduction process-technology (AOP-AOT/ARP-ART) for sustainable water and air remediation [1,2] as well as hydrogen and chemical fuels' production by water splitting and CO_2 reduction, utilizing environmentally benign materials and solar energy [3–5]. Despite its unique solar powered potential, the process efficiency is compromised by two major limitations, i.e. the persistent recombination of photogenerated charge carriers [6,7] and the poor solar light harvesting stemming from the wide band gap (3.0–3.2 eV) of titania's polymorphs [8]. An advanced, though challenging, photon management approach that directly aims at enhancing titania's ability to harness solar light is by structuring TiO_2 photocatalysts in the form of photonic crystals [9]. Photonic crystal-assisted TiO_2 photocatalysis has recently emerged as a promising structural modification to boost light harvesting of photocatalytic materials by means of slow photons i.e. light propagation at reduced group velocity near the edges of the photonic band gap (PBG) [10–13]. The underlying mechanism relies on the optimal overlap of slow photons with the targeted spectral range, where the photocatalyst' absorbance is to be enhanced, while avoiding detrimental Bragg reflection losses by tuning the PBG within the materials' electronic absorption region.

Besides amplifying the materials' photoreactivity, PBG engineering in the UV–vis spectral range results in the fabrication of macroporous periodic structures, the most common being inverse opals, which feature improved mass transport and adsorption that can be further combined with compositional modifications of the photocatalysts'

---

electronic properties for enhanced charge separation and visible light activation [14]. In particular, titania inverse opals, commonly fabricated by colloidal template self-assembly [15–17], are periodic structures that besides the refractive index periodicity that controls light propagation and their unique photonic properties, form a network of interconnected macro/mesopores of tunable size. This porous architecture affords significant improvements in the photocatalytic activity by enhancing molecular diffusion kinetics as well as increasing the surface area and the amount of adsorption and reaction sites, alike hierarchically ordered macro/mesoporous photocatalysts [18,19]. These favorable structural characteristics can be synergistically combined with targeted titania's electronic modifications, such as nonmetal and self-doping [20,21], coupling with plasmonic nanoparticles [22,23] and heterostructuring with narrow band gap semiconductors [24] or carbon nanomaterials [25,26] to simultaneously improve photon capture and photogenerated charge separation that play pivotal role in the design of highly active photocatalysts for environmental remediation and solar to chemical energy conversion applications [14].

Among the wealth of TiO_2 heterostructures, compositing titania with graphene and its derivatives has been considered a promising route to improve charge separation and light harvesting of TiO_2 photocatalysts relying on graphene materials' exceptional electron acceptor action and charge transport together with its unique two-dimensional morphology and broadband light absorption [27,28]. Among them graphene oxide (GO), the solution processable graphene precursor, has been attracting increasing attention because of its inherently rich surface chemistry and reactivity. Its lamellar structure consists of graphene sheets with randomly distributed surface oxygen groups that provide abundant anchoring sites for titania nanoparticles and thus form a highly functional platform for the fabrication $GO-TiO_2$ composites [29–31]. Hierarchically ordered macro/mesoporous graphene-TiO_2 inverse opals films were first reported by Du et al. [32] by the incorporation of GO and the Pluronic P123 surfactant in the titania sol precursor that was infiltrated in colloidal polystyrene opal templates of 240 and 300 nm diameters, followed by *in situ* GO reduction and calcination. Order of magnitude enhancement of the photocatalytic activity on methylene blue (MB) dye degradation has been reached in comparison to mesoporous TiO_2 films, which was related to the improved pollutant diffusion and interfacial electron transfer and transport between reduced GO and TiO_2. Very recently, plasmon sensitized graphene-TiO_2 photonic crystals were fabricated by Boppella et al. [33] by the sequential deposition of reduced graphene oxide and Au plasmonic nanoparticles on TiO_2 inverse opals of 500 nm void diameter, the corresponding incomplete PBG (*stop band*) of TiO_2 was anticipated at ca. 1200 nm, for photoelectrochemical water splitting. A distinct rise in the H_2 evolution rate was observed for the $Au/rGO/TiO_2$ photonic films compared to unmodified titania photoelectrodes, especially under visible light, attributed to the synergy of the Au localized surface plasmon resonance and rGO-mediated charge separation/transportation. Apart from graphene, carbon deposited TiO_2 photonic crystals were earlier reported as highly efficient visible light activated photocatalysts by means of high temperature pyrolysis of phloroglucinol/formaldehyde resol coatings onto large macropore (ca. 500 nm) titania inverse opals [34]. High rates of MB degradation were thus obtained in both aqueous and viscous polymeric solutions for high carbon loadings under visible light (495–700 nm) due to the formation of a carbon layer together with C-doping at the carbon/TiO_2 interface, which synergistically enhanced visible light absorption. Although photonic effects were hardly explored in these studies, the notably enhanced performance of these materials validates the importance of the macroporous inverse opal networks in fostering highly efficient photocatalysts and photoanodes for organics decomposition and water splitting, respectively.

Chemical exfoliation of graphite nanofibers has recently enabled size controlled synthesis of stable aqueous GO nanocolloids consisting of GO nanosheets (nanoGO) down to a few nanometers in lateral width

[35]. Compared to regular, micrometer-sized, GO sheets, the reduced dimensions of nanoGO and the concomitant higher edge-to-area ratios lead to increased surface charge density that increases their hydrophilicity and colloidal stability, which despite their promising application potential have been hardly investigated so far, the most relevant applications being in the graphene/TiO_2 core shell composites for hydrogen production [36] and hybrid biopolymer membranes for water purification [37].

In this work, surface modification of PBG engineered TiO_2 photonic crystals by GO nanocolloids was explored as an integrated approach to judiciously combine the advantages of macroporous photonic structures for improved light harvesting, surface area and transport with the enhanced adsorption capability, surface reactivity and charge separation of nanoGO to improve the performance of photocatalytic TiO_2 films. To this aim, TiO_2 inverse opals were fabricated by the co-assembly of a water soluble sol-gel titania precursor with polymer colloidal spheres following the method recently developed by Aizenberg et al. [38]. This process has been put forward as an effective means to evade liquid infiltration into preassembled opal templates and improve the quality of inverse opal films, mitigating overlayer and crack formation [39]. The interplay of slow photon effects on MB dye degradation under UV–vis and visible light with dye adsorption and interfacial electron transfer were comparatively investigated in a series of surface functionalized nanoGO-TiO_2 inverse opal films of variable macropore size for the fabrication of tailor-designed photonic catalysts.

2. Experimental

2.1. Materials and reagents

Monodisperse polystyrene (PS) spheres were purchased from Polysciences Inc. (Polybead® PS Microspheres) in the form of colloidal dispersions of 2.6% solids (w/v) in DI water with diameters of 220 (8% CV, SD = 0.02 μm), 350 (3% CV, SD = 0.01 μm) and 510 nm (5% CV, SD = 0.01 μm) as well as 425 nm (5% solids, 2.3% CV, SD = 0.01 μm) from Microparticles GmbH (Berlin, Germany). Titanium(IV) bis(ammonium lactato)dihydroxide (TiBALDH) 50 wt.% aqueous solution, graphene oxide nanocolloids (2 mg/ml dispersion in H_2O), graphene oxide sheets (2 mg/ml dispersion in H_2O) and Hellmanex™ III were purchased from Sigma Aldrich. All other reagents were of analytical or ACS reagent grade: ethanol (absolute, 99.8%), acetone (ACS reagent, reag. ISO, reag. Ph. Eur., ≥99.5%), hydrochloric acid (ACS reagent, reag. ISO, reag. Ph. Eur., fuming, ≥37%).

2.2. Inverse opal fabrication and surface modification

Titania inverse opal films were fabricated by the convective evaporation-induced self-assembly (EISA) technique employing the co-assembly of sacrificial PS colloidal spheres (diameters of 220, 350, 425, 510 nm) with a hydrolyzed titania sol-gel precursor [38]. In a typical deposition, cleaned (Hellmanex™ III, ultrasound acetone-EtOH) glass slides were vertically suspended in a vial containing 8 ml of 0.2 wt% diluted PS sphere suspension in Milli-Q water and 0.168 ml of fresh titania precursor (1.23 ml TiBALDH solution, 1.5 ml HCl 0.1 M and 2.85 ml EtOH), both sonicated for 30 min prior to use. The vials with the suspended glass substrates were kept at 55 °C until the solvent fully evaporated over a period of 3 days, yielding composite films comprising the titania gel distributed within the interstices of the close packed PS opal structure. The dry films were then calcined at 500 °C for 2 h in air at a heating rate of 1 °C/min, to remove the polymer matrix and crystallize titania in the inverse opal structure. The obtained TiO_2 photonic crystals are designated as PC220, PC350, PC425 and PC510 after the diameter of the PS colloidal spheres. Disordered TiO_2 inverse opals (designated as PCmix) were assembled using a mixture of the 350, 425 and 510 nm PS spheres at equal weights (2.67 ml of 0.2 wt% PS colloidal suspension), in order to disrupt the films' long range periodicity

and PBG generation, while preserving their macroporous structure. PCmix were accordingly used as reference films to attest slow photon effects. In addition, mesoporous TiO_2 reference films were deposited on glass slides by the doctor blade technique using a paste of the benchmark Aeroxide® P25 (Evonik) titania nanopowder in order to validate the photonic materials' performance.

Surface modification was subsequently performed by dipping the inverse opal and P25 TiO_2 films for 24 h in the GO nanocolloidal dispersion (2 mg/ml in H_2O), whose pH was stabilized at 10 by adding periodically a few drops of dilute NaOH aqueous solution [40,41]. The functionalized TiO_2 photonic films were named as nanoGO-PC220, nanoGO-PC350, nanoGO-PC425, nanoGO-PC510 and nanoGO-P25. The same procedure was applied for the PC350, PC425 and PC510 inverse opals using a regular GO dispersion (2 mg/ml in H_2O) containing micrometer-sized (mean sheet diameter of 22 μm) GO sheets, in order to explore size effects arising from the GO sheet lateral dimensions. The corresponding films were designated as GO-PC350, GO-PC425 and GO-PC510.

2.3. Materials characterization

The films' morphology was characterized using a FEI Quanta Inspect Scanning Electron Microscope (SEM). The nanostructure as well as materials phase composition was studied by an FEI CM20 High Resolution Transmission Electron Microscope (HR-TEM) equipped with a Gatan GIF 200 Energy Filter. The materials structural properties were determined by micro-Raman spectroscopy using a Renishaw inVia Reflex microscope with a solid state laser and a laser diode emitting at 514 and 785 nm, respectively. The laser beam was focused onto the samples by means of a ×50 (NA = 0.75) objective on a Leica DMLC microscope, while the laser power density was kept at low levels (0.05 mW/μm²), especially for the dye sensitized titania films (< 0.004 mW/μm²) to avoid local heating and dye degradation under laser irradiation.

Low-pressure nitrogen (77.4 K), adsorption measurements were performed on an Autosorb 1-MP volumetric system (Quantachrome Inc. USA), with Krypton upgrade using approximately 10 mg of powder samples scrapped from the inverse opal films, while the measuring temperature was fixed by means of a dewar flask containing liquid nitrogen. Ultra-high purity N_2 (99.999%), was used for all adsorption measurements, while helium (99.999%) was used for volume calibrations. Prior to analysis, the samples were outgassed for 24 h at 160 °C under high vacuum.

The surface area was evaluated utilizing the multipoint BET (Brunauer Emmet Teller) method. The pore size distributions (PSDs) of the macroporous periodic structures in the inverse opal films were obtained from the desorption branch of the isotherm, involving the Barrett, Joyner and Hallenda analysis. The mean pore size (d_{mean}) for spherical pore geometry was calculated by the total pore volume (TPV) at $P/P_0 = 0.995$ and the BET surface, applying the equation $d_{mean} = 6 \cdot (TPV)/(BET)$. NLDFT – N_2 – silica adsorption branch kernel at 77 K based on a cylindrical pore model for pores of diameter < 5 nm, and spherical pores of diameter > 5 nm and NLDFT – N_2 – silica equilibrium transition kernel at 77 K based on a cylindrical pore model (0.35–100 nm) were employed to study the pore structure of the solid skeleton in the inverse opal films and derive the respective PSDs.

Electron paramagnetic resonance (EPR) measurements were performed on an upgraded X-band Bruker ER-200D spectrometer interfaced to a personal computer and equipped with an Oxford ESR 900 cryostat, an Anritsu MF76A frequency counter and a Bruker 035 M NMR gaussmeter. The Signal-Channel unit was replaced with an SR830 digital lock-in amplifier by Stanford Research. Scrapped powder samples of the same mass (∼ 5 mg) were filled in quartz tubes and cooled at 12 K, where illumination was directly performed in the perpendicular 4102ST cavity using 360 W/82 V tungsten halogen lamp equipped with a water filter to remove IR radiation and a UVA Sylvania 15 W/BLB

lamp emitting at 350–390 nm (~ 0.5 mW cm^{-1}). The EPR spectra were typically recorded at microwave frequency of ∼ 9.42 GHz and modulation amplitude of 4 Gpp at 100 kHz, with microwave power of 20 mW.

Optical spectra of the titania films were recorded on an Agilent Cary 60 UV–vis spectrophotometer with the focused beam (1.5 mm × 1.0 mm) of a Xenon flash lamp (80 Hz) in the range of 200–1000 nm. Diffuse reflectance spectra were acquired from the film surface (spot size of 1.5 mm) using the Agilent Cary 60 remote diffuse reflectance accessory together with the corresponding fiber optic coupler, while specular reflectance was obtained at 15° utilizing a slide mounted specular reflectance accessory (PIKE, UV–vis 15Spec). Baseline reflectance spectra were acquired by a Halon standard and a UV Al mirror, respectively. Photoluminescence (PL) measurements were carried out by lock-in amplification techniques. The focused beam of a light-emitting diode at 275 nm was used for excitation and modulated by a mechanical chopper. The modulated PL signal was analyzed by an Oriel 77200 1/4 monochromator and detected by a Si photodiode using a PDA200C Benchtop Photodiode amplifier (Thorlabs). The modulated PL signal was fed into the lock-in amplifier and the recovered PL signal from the background noise was recorded using LabView and corrected to the system's response.

2.4. Photocatalytic performance

The photocatalytic activity of the photonic and reference materials was evaluated on the aqueous phase degradation of methylene blue [3,7-bis(dimethylamino)phenazathionium chloride] (MB) (Alfa Aesar A18174). The photocatalytic experiments were carried out in beaker containing 4 ml of 3 μM aqueous MB solution and the titania films of 1.5 cm² area. Before illumination, the films were left in the MB solution to reach adsorption-desorption equilibrium under dark conditions. The equilibration time was determined by monitoring the MB adsorption kinetics on representative TiO_2 films, namely PC425, nanoGO-PC425, P25 and nanoGO-P25 TiO_2 (Fig. S1 in Supplementary material). The amount of dye adsorption q_t at time t was quantified as $q_t = \frac{[C(0) - C(t)] V}{M}$ in units of mg(MB)/g(TiO_2), where $C(0)$ and $C(t)$ are the concentrations of the dye solution at times $t = 0$ and $t \neq 0$ in the dark, V is the dye solution volume and M is the mass of the TiO_2 adsorbent, estimated by weighting the glass substrates before and after the co-assembly and calcination of the inverse opals. In all cases, the dye uptake on the TiO_2 film surface rapidly reached equilibrium within the first 30 min, as can be seen in Fig. S1 (Supplementary material), in agreement with previous results on macro/mesoporous graphene-TiO_2 films [32]. A contact time of 30 min was accordingly selected for dark equilibration. It is worth noting that besides the marked increase of MB adsorption, nanoGO functionalization resulted in a slow temporal rise of q_t for long times, reaching ca. 3% after 240 min [Fig. S1(b)], which, nevertheless, had negligible effects in the photocatalytic degradation kinetics monitored within a shorter time period $t \leq 110$ min. MB photocatalytic degradation was subsequently performed under illumination by a 150 W Xe lamp (ORIEL 6255). UV–vis irradiation was selected by the combination of a long-pass edge filter with cut-on wavelength of 305 nm (Newport 20CGA-305) and a heat reflective mirror (Newport 20CLVS-3 CoolView™, T_{avg} = 85% at 332–807 nm, R_{avg} = 95% at 840–1500 nm). Visible light irradiation was selected by an additional long-pass edge filter with cut-on at 400 nm (Newport 20CGA-400). The horizontal Xe beam was directed to the photocatalytic film at the vial bottom via a UV-enhanced broadband Al mirror (Newport ValuMax 20D520AL.2, λ/10, R_{avg} > 90% at 250–600 nm) delivering 2.8/2.1 mW/cm² of incident irradiation on the film surface in the UV–vis/Vis spectral ranges, respectively. A small (0.5 ml) aliquot of the MB solution was withdrawn at given time intervals and quantitatively analyzed using a 10 mm path length quartz micro cell (HELMA Analytics 105B-QS, 500 μL) in the Cary 60 spectrophotometer.
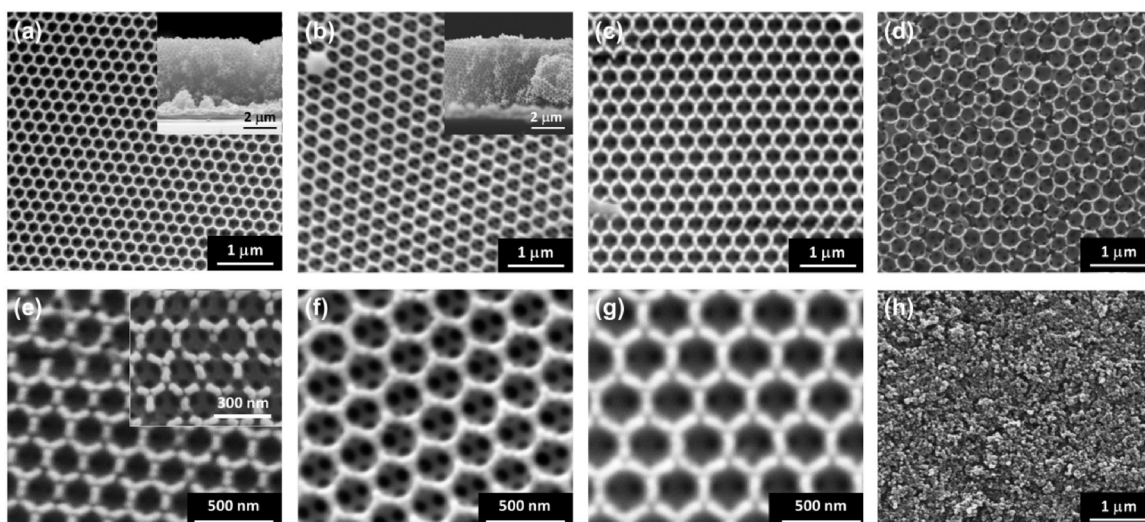
Fig. 1. SEM images of the (a,e) PC350, (b,f) PC425, (c, g) nanoGO-PC510, (d) PCmix inverse opals and (h) P25 TiO_2 films at different magnifications. The insets in (a) and (b) show cross sections of the PC350 and PC425 films, respectively. The inset in (e) shows the macropores of the PC220 film.

Subsequently, the analyzed aliquot was poured back into the reacting solution. The photocatalytic conversion ratio is denoted as C/C_0, where C_0 is the adsorption equilibrium concentration of the MB solution and C is the concentration at time t. The stability of the photocatalytic films was tested by repeating three times the UV–vis MB degradation experiment for the same film, which after each cycle was rinsed with water and dried under N_2 flow.

3. Results and discussion

3.1. Morphology, phase composition, texture and optical properties

Fig. 1 shows representative SEM images of the co-assembled TiO_2 inverse opal films that disclose the formation of highly ordered three dimensional (3D) close packed structures corresponding to the (111) planes of an *fcc* lattice consisting of void spheres within the titania framework. On the other hand, long range periodicity was suppressed in the PCmix films that formed from the packing of spheres of different diameters [Fig. 1(d)], while reference P25 films presented a rough, sponge-like morphology, characteristic of mesoporous films [Fig. 1(h)]. The hexagonally arranged macropores in the inverse opals were well interconnected through smaller pores of 40–90 nm, corresponding to the dark contrast circular areas, most clearly seen in the high magnification SEM images of Fig. 1. The latter emerge at the contact points between adjacent PS spheres after calcination [42] and are essential for the confined transport and diffusion kinetics of pollutant molecules within the porous structure [43,44]. The average macropore size of the inverse opal films was ca. 56% of the original PS colloidal sphere diameter, namely 140(1), 200(10), 240(10) and 280(10) nm for the PC220, PC350, PC425, PC510 films, respectively (Table 1), indicative of considerable shrinkage after calcination, while the film thickness was ca. 4 μm, as shown by the cross section SEM images in the insets of Fig. 1(a) and (b). Low magnification SEM images, attest that co-assembly yields long range ordered inverse opal films, free of compact overlayers with typical domains extending over ca. 20–50 μm, as shown in Fig. S2 (Supplementary material). However, cracks are still observed due to the calcination-induced cracking that persists in crystalline metal oxides via the amorphous-to-crystalline phase transition and the associated volume shrinkage of the inorganic matrix after thermal treatment [45]. Surface functionalization with the nanoGO dispersion had no observable effect on the film morphology and macrostructure, leaving intact the macropore ordering, as shown for nanoGO-PC510 in Fig. 1(c) and (g).

Table 1

Structural and optical properties of the TiO_2 inverse opal films.

Sample	D_{PS}[a] (nm)	D[b] (nm)	λ_{exp} (15°)[c] (air)	n_{eff} (air)	$1 - f$	n_{eff} (H_2O)	λ_{th} (0°)[d] (air)	λ_{th} (0°)[d] (H_2O)
PC220	220	140	330	1.47	0.209	1.66	335	380
PC350	356	200	420	1.31	0.131	1.55	428	505
PC425	425	240	530	1.38	0.163	1.59	540	625
PC510	510	280	625	1.39	0.170	1.60	636	734

[a] D_{PS} = diameter of the colloidal PS spheres.

[b] D = macropore diameter of the TiO_2 inverse opal films determined by SEM.

[c] λ^{exp} = stop band wavelength determined from the 15° incidence specular spectra.

[d] λ^{th} = stop band wavelength predicted from modified Bragg law for θ = 0° incidence angle.

The inverse opal structure was further investigated by TEM, as shown in Fig. 2(a), where bright contrast represents the ordered void macropores, while dark contrast corresponds to the solid skeleton walls. TEM images of the PC425 samples at different tilt angles (−45° to +45°), shown in Fig. S3 (Supplementary material), clearly demonstrate the 3D spatial cell morphology of the inverse opal. HR-TEM images at successively higher magnifications, shown in Fig. 2(b)–(d), reveal that the skeleton walls consist of 5–10 nm crystalline nanoparticles with distinct *d*-spacings, the most common being the 0.35 nm lattice fringes corresponding to the (101) planes of the anatase TiO_2 phase [inset of Fig. 2(d)].

Energy-filtered TEM (EFTEM) elemental mapping was further applied in order to prove the presence of nanoGO on the surface of the modified titania films utilizing the three-window method. Fig. 2(f), (g) and (h) shows characteristic C, O and Ti elemental maps of the area shown in the bright field TEM image of Fig. 2(e), for the nanoGO-PC425 sample. The presence of GO nanosheets deposited on the nanocrystalline TiO_2 walls of a void macropore can be directly identified, verifying the formation of firm nanoGO-TiO_2 interfaces and successful functionalization of the TiO_2 inverse opals. Moreover, analogous EFTEM elemental maps at different magnifications on GO-PC425 and GO-PC510 films subjected to surface functionalization by regular, micrometer GO sheet dispersion indicates more extensive coverage of the nanocrystalline titania walls by the GO sheets that spread over more than one void micropore (Figs. S4 and S5 in Supplementary material). This may partially block the pore accessibility to the diffusing pollutant molecules and thus impose an adverse effect to the photocatalytic process.
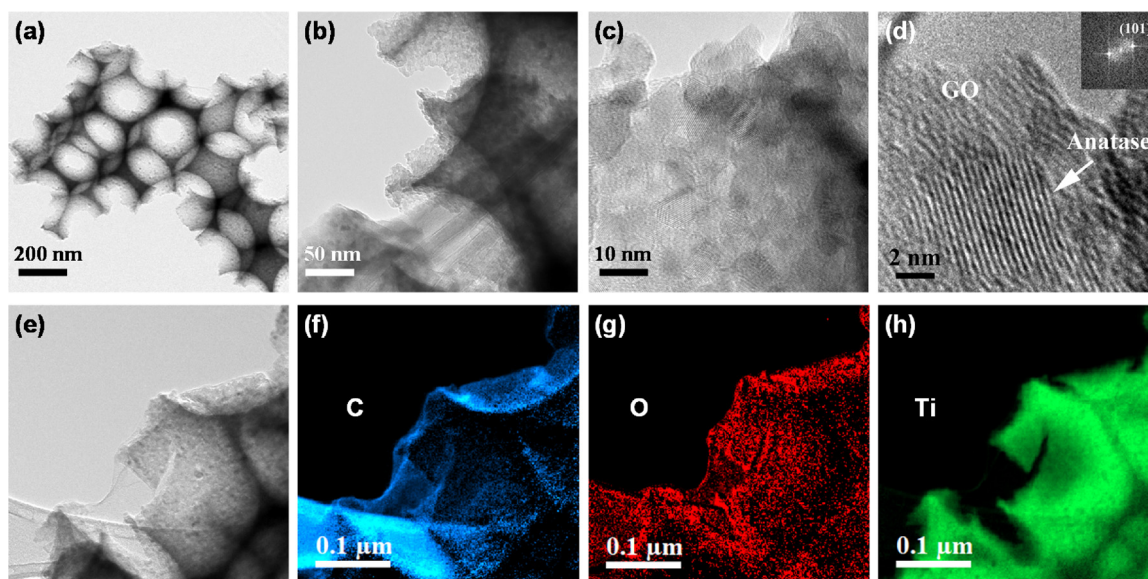
Fig. 2. (a)-(c) TEM images of the PC425 sample at different magnifications. (d) HR-TEM image of nanoGO-PC425 showing (101) anatase lattice fringes. The inset shows the corresponding FFT analysis of an anatase nanoparticle embedded within the GO nanosheets. (e) Bright field image of nanoGO-PC425 and the corresponding (f) C, (g) O and (h) Ti EFTEM elemental maps.
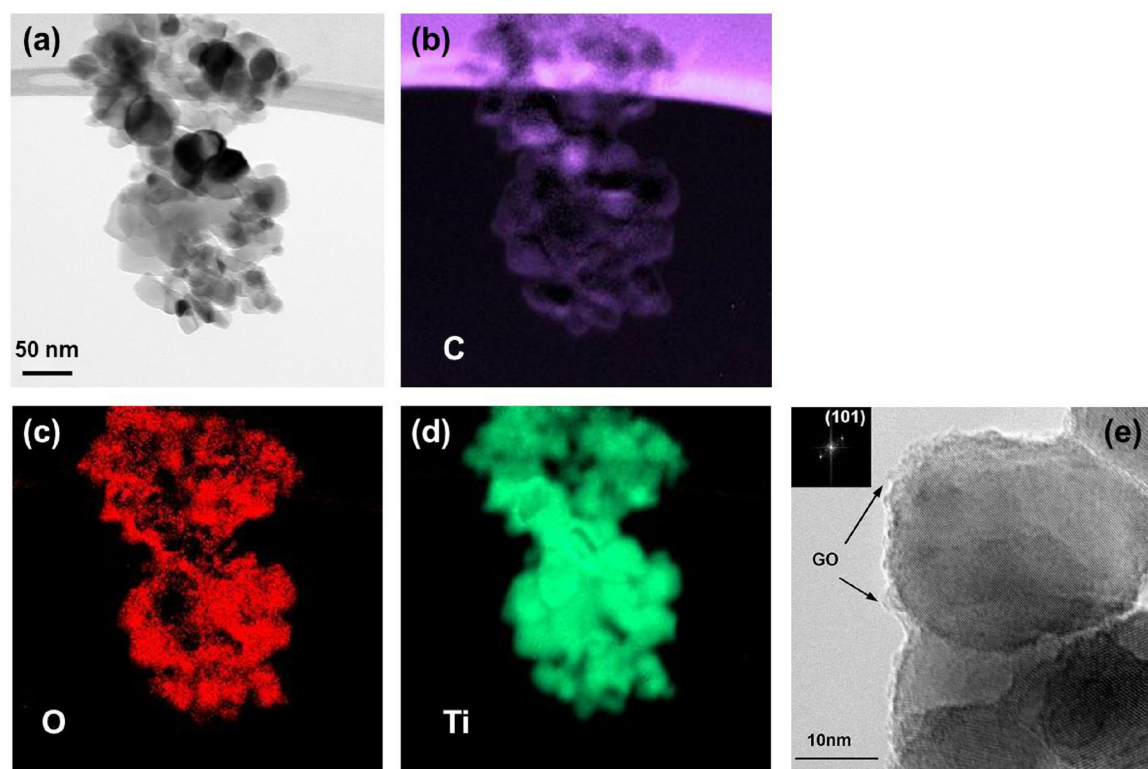

Fig. 3. (a) Bright field TEM image of nanoGO-P25 nanoparticles and the corresponding (b) C, (c) O and (d) Ti EFTEM elemental maps. (e) HR-TEM image and FFT analysis of adjacent titania nanoparticles covered by GO shell.

This was most essential for the nanoGO-P25 films, where GO nanosheets were observed to cover extensively the TiO_2 nanoparticles according to the EFTEM elemental maps shown in Fig. 3(a)–(d). In that case, HR-TEM imaging indicated that the GO shell may spread over the narrow mesopore space among the titania (anatase mainly) nanoparticles, as shown in Fig. 3(e), and thus inhibit diffusion of pollutant molecules through the whole film thickness during aqueous phase photocatalysis.

The structural characteristics and phase composition of the inverse opals were further investigated by Raman spectroscopy. Fig. 4(a) compares the Raman spectra of the nanoGO functionalized PC and P25 films at 514 nm. All PC samples (including the unmodified pristine photonic films) exhibited the characteristic Raman-active phonon modes of the anatase TiO_2 at approximately 148 (E_g), 199 (E_g), 398 (B_{1g}), 520 ($A_{1g} + B_{1g}$), and 643 cm^{-1} (E_g) [46]. No trace of polystyrene remnants or other titania polymorphs such as rutile or brookite could be identified, confirming that all inverse opal films calcined at 500 °C, crystallized in the anatase phase, in agreement with the TEM analysis.

(a)

(b)   (c)
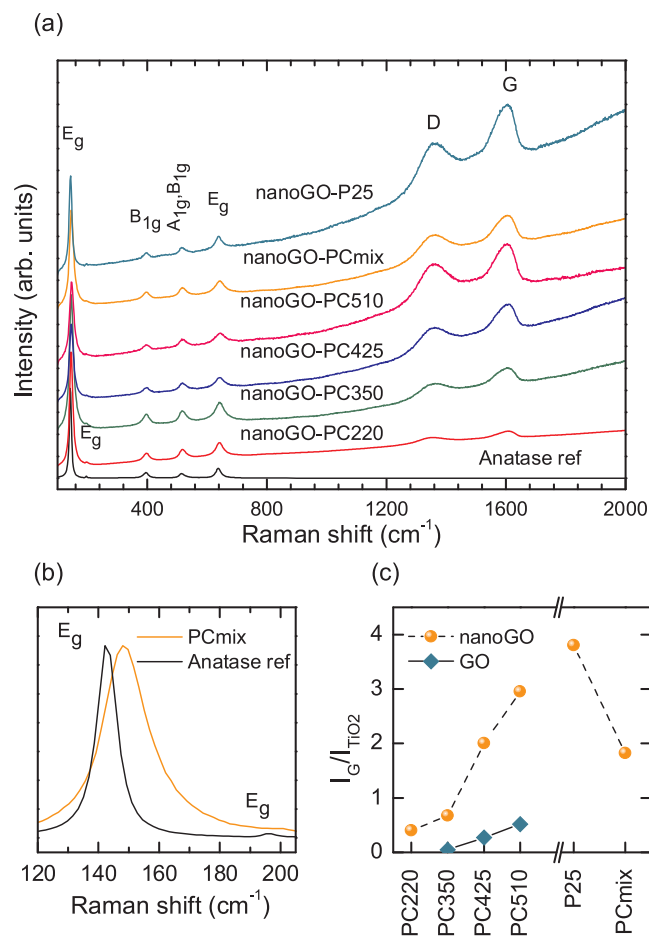
Fig. 4. (a) Raman spectra of the nanoGO-PC and P25 inverse opal films compared to an anatase reference at 514 nm. (b) The lowest frequency E_g anatase mode for the PCmix, P25 and anatase reference films. (c) The variation of the integrated intensity ratio I_G/I_{TiO2} for the surface functionalized photonic films in nanoGO and regular GO dispersions.

Furthermore, appreciable broadening and shift of the anatase Raman peaks was observed, compared to an anatase reference film, deposited by the doctor blade technique on glass using a paste of large ($> 100\,nm$) anatase particles [47]. The most intense, low frequency E_g anatase mode shifted to higher wavenumbers ($148\,cm^{-1}$) and broadened considerably to a full-width at half-maximum (FWHM) of $18\,cm^{-1}$, compared to the reference sample ($142.5\,cm^{-1}$ with FWHM = $8\,cm^{-1}$) that approaches bulk behavior, as shown in Fig. 4(b). This variation can be explained by the size effects arising from the breakdown of the $q = 0$ Raman selection rule by means of optical phonon confinement that leads to the broadening and blue shift of the Raman bands for nanomaterials [48]. Application of the frequency vs FWHM correlation curves derived by the application of the phonon confinement model for the E_g anatase mode [49,50], indicate the formation of anatase nanocrystals of ca. 7 nm, in close agreement with the direct TEM observations. Despite the relatively high calcination temperature (500 °C), the size of the anatase nanocrystals is rather small. This can be mainly related to the lactate ligands of the water soluble TiBALDH precursor that inhibit crystal growth [51–54] as well as the confined sol-gel reaction within the opal interstices. where liquid infiltration using conventional titanium alkoxide precursors such as titanium isopropoxide or butoxide also impedes particle growth and the anatase-rutile transformation [55–57].

Besides the anatase vibrational bands, the nanoGO functionalized films presented the characteristic defect activated D and tangential G Raman modes of GO at 1347 and $1600\,cm^{-1}$, respectively. In

particular, the G band that stems from the stretching of sp^2 carbon atoms, exhibited the distinct GO asymmetric lineshape, where spectral weight is shifted to the high frequency side, reflecting the contributions of alternating single-double C bonds [58]. Moreover, the relative intensity of the GO bands presented a marked evolution with the inverse opal macropore size with respect to the anatase modes, indicating that the loading of nanoGO on the TiO_2 photonic crystals increased with the enlargement of the void diameter. Quantification of this variation using the intensity ratio of the integrated area of tangential G mode relative to the most intense E_g anatase mode I_G/I_{TiO2} indicated a four-fold increase of nanoGO loading from PC350 to the PC510 inverse opals with a small recovery for PC220 [Fig. 4(c)]. However, it should be noted that multiple scattering via slow photons and Bragg reflection of the excitation laser beam at 514 nm [59] for the PC350 and PC425 inverse opals (*vide infra* Section 3.2) may increase/decrease the apparent Raman intensity of the GO modes and the corresponding I_G/I_{TiO2} ratios, leading to over/underestimates of the GO loadings for these films, respectively. An even higher I_G/I_{TiO2} ratio was observed for the nanoGO-P25 films complying with the high surface coverage of the titania nanoparticles by GO nanosheets observed by TEM (Fig. 3).

Furthermore, Raman spectra of photonic films functionalized in regular, GO sheet dispersion (Fig. S6 in Supplementary material) exhibited appreciably lower intensity I_G/I_{TiO2} ratios by a factor of 5–10, as shown in Fig. 4(c). This indicates that GO nanosheets are favorably adsorbed on the nanocrystalline walls of the titania inverse opals due to their reduced lateral dimensions. In the case of normal GO, the high frequency 2D overtone at $\sim 2700\,cm^{-1}$ and the D + D' combination mode at $\sim 2930\,cm^{-1}$ could be better resolved compared to the nanoGO functionalized films due to the relative suppression of the intense GO photoluminescence that usually masks the Raman spectra of pristine GO, further signifying the interfacial coupling of GO with the TiO_2 nanocrystallites [60].

Fig. 5 shows the UV–vis specular (R%) and diffuse (DR%) reflectance spectra of the TiO_2 inverse opal and P25 films, before and after surface functionalization by the GO nanocolloids. A broad but distinct peak (represented by the hatched band in Fig. 5) was resolved in all the 15° incidence R% spectra that shifted strongly to lower wavelengths with the decrease of the inverse opal macropore size, in contrast to the weak band arising from the anatase electronic band gap absorption at 375 nm and the featureless spectra of the disordered PCmix and P25 films. This variation is characteristic of the pseudo-PBG (stop band) formation for wave propagation along the ΓL-direction in reciprocal space, i.e. the [111] crystal direction in real space, of TiO_2 inverse opals with variable macropore diameters [14]. The photonic stop bands at 15° incident angle were accordingly identified at 330(10), 420(10), 530(10) and 625(10) nm for the PC220, PC350, PC425, PC510 inverse opal films, respectively (Table 1). Their spectral positions can be approximated by modified Bragg's law for first order diffraction from the (111) planes, defined as [61]:

$$\lambda = 2d_{111}\sqrt{n_{eff}^2 - \sin^2\theta}$$

where λ is the stop band wavelength, $d_{111} = a/\sqrt{3} = \sqrt{2/3}D$ is the interplanar spacing of the (111) crystal planes with a being the cubic lattice constant and D the macropore diameter, n_{eff} is the volume-weighted average of the spheres' refractive index n_{sphere} and the material n_{solid} occupying the solid skeleton, defined by $n_{eff}^2 = n_{sphere}^2 f + n_{solid}^2(1 - f)$ with f being the filling fraction ($f = 0.74$ for the fcc lattice) and θ is the angle between the incident beam and the plane normal. Using $\theta = 15°$ together with the measured stop band positions and macropore diameters for $n_{TiO2} = 2.55$ and $n_{air} = 1.0$, n_{eff} values of ca.1.4 and skeleton filling fractions ($1 - f$) of 0.17 were determined in air (Table 1), in agreement with previous results on well-ordered titania inverse opals prepared by liquid infiltration [62].

This pronounced spectral variation with the films' macropore size was directly confirmed on the corresponding DR% spectra (Fig. 5).
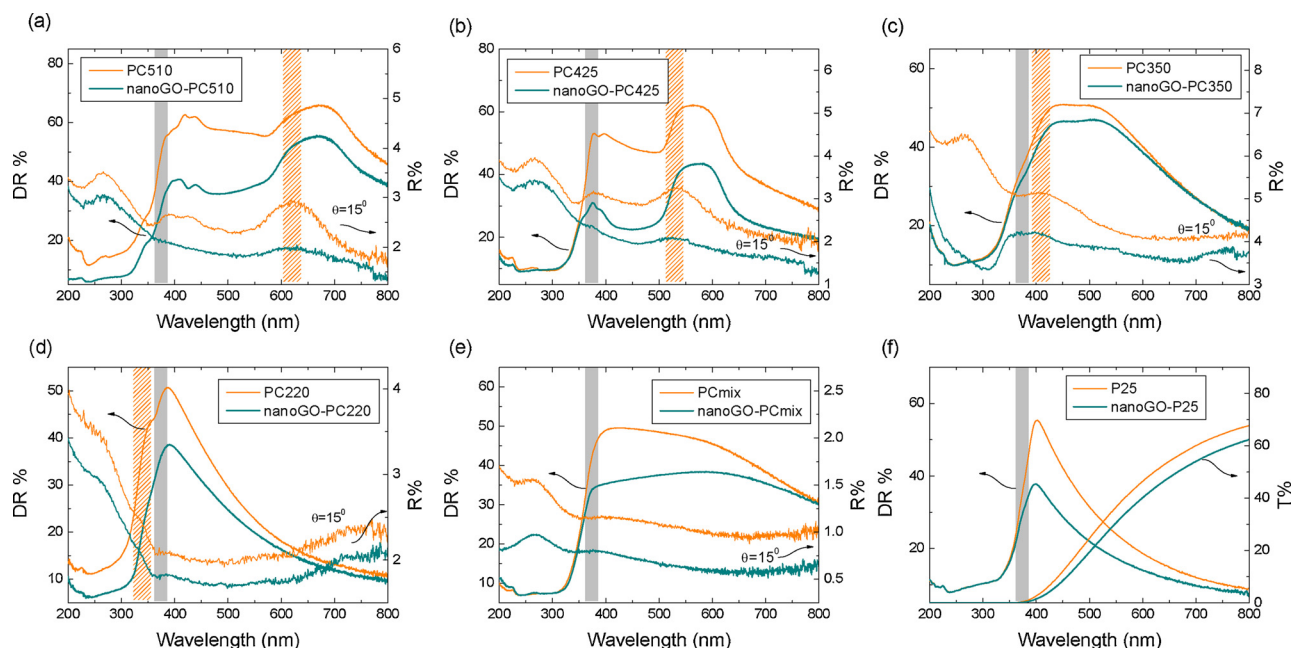
Fig. 5. UV–vis specular (R%) and diffuse (DR%) reflectance spectra of the TiO$_2$ inverse opal and P25 films before and after surface functionalization by the GO nanocolloids. Hatched and shaded bands designate the photonic stop bands at 15° incident angle and the electronic anatase band gap absorption, respectively.

However, the DR intensity largely exceeded the specular one, indicating the presence of disorder with respect to the relatively coarse (1.5 mm^2) spot of the focused (not collimated) light beam that probes film areas comprising several domains of different thickness and surface flatness. Moreover, the broader and anisotropic DR% peaks were systematically red shifted toward the low energy (red) edge of the corresponding stop bands at wavelengths considerably higher than those predicted by the 15° incidence specular spectra (Table 1). This behavior can be rationalized as slow photons at the stop band edges experience a longer optical path, which thus increase the probability for light scattering by lattice disorder [63,64] within the area probed by the coarse beam. This can enhance diffuse reflectance at the PBG edges, contrary to frequencies close to the stop band center, where the attenuation of light penetration inhibits intense diffuse scattering [65]. This effect appears to be most relevant to the red stop band edge, where slow photons are expected to localize in the high dielectric part of the inverse opal i.e. the titania skeleton, leading to the pronounced asymmetry of the DR% spectra, which may thus become a sensitive probe of "red" slow photons. In addition, high energy reflectance peaks were observed in the larger macropore inverse opals, most prominent in the intense DR% spectra of the PC510 film as a double-peaked band at 420–440 cm^{-1}. High energy PBG features have been rarely observed in titania inverse opal films, such as those fabricated by atomic layer deposition [66], indicating the high quality of the co-assembled photonic films. Deposition of nanoGO on the titania films resulted invariably in the broadening of all photonic features due to the broadband absorption of the GO nanosheets [35] that partly reduced both specular and diffuse reflectance. On the other hand, the stop band positions of the functionalized films remained practically constant, reflecting the small influence of the GO nanosheets on the inverse opal macropores, in agreement with the intact periodicity of the nanoGO-TiO$_2$ films observed by SEM. Likewise, both DR% and transmittance spectra of the P25 films decreased after nanoGO deposition, reflecting its broadband absorption.

The pore structure and texture properties of the titania inverse opals derived from the analysis of the low-pressure nitrogen (77.4 K) adsorption shown in Fig. 6, are summarized in Table 2. The BET surface area was found to vary in the range of 39–49 (m^2/g) in agreement with previous reports on both inverse opal powders and films [57,63,67].

Nevertheless, these BET values were appreciably high to be solely attributed to the macroporous structure of the inverse opals. It is rather the nanoporosity of the skeleton walls consisting of the inter-crystalline void space, which contributes significantly to the surface area enhancement.

As shown by the results of Table 2, the mean pore size (d_{mean}) derived by assuming spherical macropores is underestimated compared to the pore size determined by the SEM analysis (Table 1). This deviation can be rationalized by the fact that the calculated BET encompasses both the wall surface of the macropores and the internal surface of the nanoporous TiO$_2$ skeleton. Similar behavior is observed in the pore size distributions (PSDs) derived from the BJH analysis of the desorption branch (Fig. S7 in Supplementary material) with the pore size centered around 100 nm for most samples (Table 2), when the minimum macropores derived by SEM for PC220 was 140 nm. In this context, the attenuation of BET surface area with the increase of the macropore size can be related to the thinning of the nanostructured skeleton with respect to the spherical void space [32]. Moreover, the effect of nanoGOs' deposition on the BJH derived pore dimension is similar for samples PC425 and PC510, subjected to a 5% and 6% reduction, respectively. On the contrary, nanoGO had a prominent negative impact on the BET surface for PC425, indicating that the GO nanoflakes inhibited the diffusion of N$_2$ to the inter-crystalline pores of the solid skeleton. Furthermore, the NLDF-derived PSDs of the PC220, PC350, PC425, PC510 and the respective GO modified samples (either adsorption or equilibrium) did not differ substantially, exhibiting two major peaks centered on pore sizes of 5 and 8 nm (Fig. S8 in Supplementary material) that are close to those expected for the inter-crystallite space of ~ 10 nm TiO$_2$ nanoparticles.

3.2. Photocatalytic activity

Fig. 7(a)–(c) compares the aqueous phase MB photodegradation kinetics for all the pristine and nanoGO functionalized inverse opal and reference films under UV–vis light. In all cases, MB photodegradation followed pseudo first-order kinetics, as can be evidenced by the linear ln(C/C_0) vs t plots in Fig. 6(b), from which the apparent rate constants k_{UV-Vis} were derived. The obtained values are summarized together with the corresponding MB adsorption (%) under dark conditions in
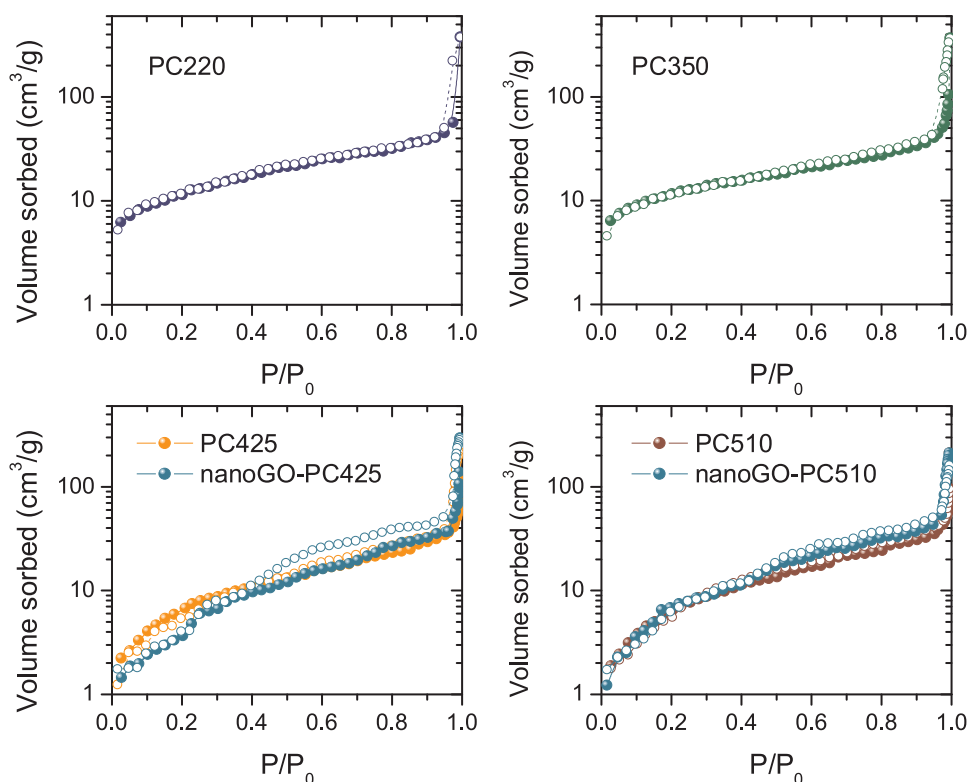
Fig. 6. Adsorption–desorption N_2 isotherms for the PC220, PC350, PC425, PC510, nanoGO-PC425, nanoGO-PC510 inverse opals at 77.4 K.

Table 2
Pore structure characteristics of the TiO_2 inverse opals.

	BET (m²/g)	TPV[a] (ml/g)	d_{mean}[b] (nm)	d_{BJH}[c] (nm)	$dNLDFT\_A$[d] (nm)	$dNLDFT\_D$[e] (nm)
PC220	48.9	0.58	71	58.2	4.6	5.3
PC350	44.4	0.57	77	88.6	4.0	5.7
PC425	37.1	0.37	60	90.6	5.0	5.1
PC510	38.8	0.33	51	105.9	5.3	5.9
nanoGO-PC425	17.6	0.46	155	84.4	5.4	6.1
nanoGO-PC510	38.4	0.25	39	100.7	4.7	5.7

[a] Total pore volume.
[b] The mean pore size d_{mean} is derived as $d_{mean} = 6 \cdot (TPV)/(BET)$.
[c] The pore size determined from the PSDs using BJH analysis of the N_2 desorption branch.
[d] The nanopore size derived from the PSDs using the NLDFT-N_2-silica adsorption branch kernel at 77 K.
[e] The nanopore size derived from the PSDs using the NLDFT – N_2 – silica equilibrium transition kernel at 77 K.

Fig. 6(c).

Significant increase of the dye adsorption was thereby evidenced on the pristine TiO_2 inverse opals reaching a maximum for the PC425 film, which can be related to the optimal combination of sufficiently large macropores and mesoporosity derived by the corresponding NLDFT-PSDs (Fig. S8 in Supplementary material) that facilitate the accessibility of the diffusing MB molecules to the internal film surface from the corresponding liquid/solid interface [32]. More importantly, dark adsorption was distinctly increased upon surface functionalization by nanoGO, most prominent for PC425 (×1.55) and PC510 (×1.7) with the higher loadings, reflecting the rich surface functionality of GO nanocolloids. In particular, the negatively charged surface oxygen groups, i.e. hydroxyl (−OH) and carboxyl (−COOH) groups of GO can favorably interact with cationic dyes such as MB that bear positively charged amino groups, while electrostatic interactions can be further assisted by means of π-π coupling of the GO itinerant sp^2 electrons with the

corresponding delocalized electrons in the aromatic rings of the dye molecules [68]. Comparative MB adsorption/photodegradation experiments on GO-PC510 inverse opals functionalized in regular GO dispersion containing larger, micrometer-sized sheets (Fig. S9 in Supplementary material) verify that the exceptional adsorptive capacity of GO is appreciably enhanced in the case of nanoGO, whose higher edge-to-area ratios increase the density of oxygen functional groups and surface charge density [35]. On the other hand, P25 and nanoGO-P25 films presented considerably high MB adsorption, exceeding the photonic films, which reflected its favorable surface reactivity and mesoporosity as well as the high nanoGO coverage inferred from TEM (Fig. 3) and Raman measurements (Fig. 4).

Following dark adsorption, a distinctive macropore size dependence of the MB photodegradation kinetics and the corresponding rate constants k_{UV-Vis} was observed for the pristine photonic films, as shown in Fig. 7(a)–(c). Among them, PC425 presented the best performance surpassing even the benchmark mesoporous P25 films (by roughly 11%). This prominent effect complied favorably with the slow photon amplification in dye sensitized TiO_2 photocatalysis reported by Li and coworkers for both TiO_2 [67] and ZnO [69] photonic crystal films. Matching the stop bands of TiO_2 inverse opals in water to the absorption bands of selected dye pollutants in the visible spectral range, was reported to result in a significant rise of the dye photodegradation rates under both visible and UV–vis irradiation. Specifically, titania inverse opals with stop bands at 530 and 660 nm in air and water, respectively, presented the highest MB photodegradation rate, especially under visible light. This was attributed to the overlap of the 664 nm MB absorption with both red- and blue-slow photon regions that enhanced the self-sensitized photocatalytic oxidation of MB molecules grafted at the interface of the high (titania) and low (water) dielectric media. In the present case, applying the modified Bragg law for the titania filling fractions $(1 − f)$ determined from the 15° incidence specular spectra (in air) and $n_{H_2O} = 1.33$, the corresponding n_{eff} values and stop band positions in water were calculated for the inverse opal films, as shown in Table 1. Among them, the 625 nm stop band for PC425 (in water)
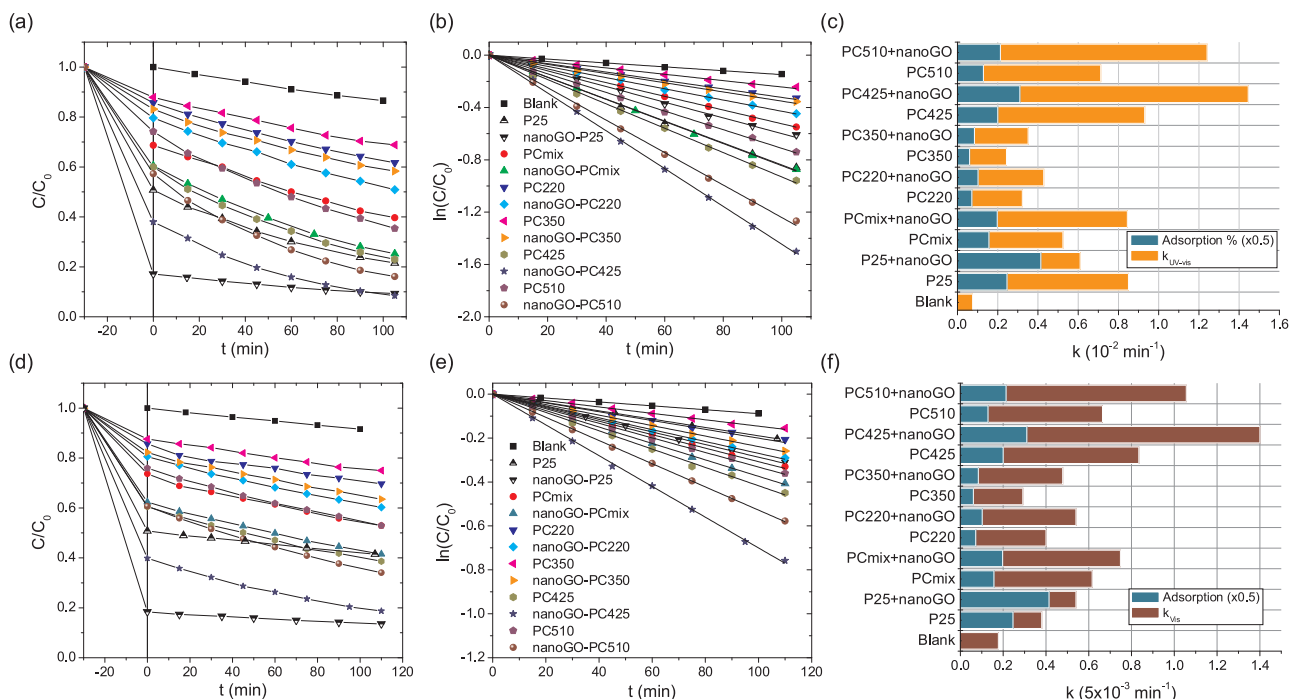
Fig. 7. MB photodegradation kinetics for the pristine and nanoGO functionalized inverse opal and reference films and the corresponding dark adsorption (%) and apparent rate constants k under (a)-(c) UV–vis and (d)-(f) visible light illumination.

approached closely the MB absorption band at 664 nm, located toward the red edge of the titania stop band, where enhanced diffuse reflectance and multiple scattering for the slow photons localized in the titania skeleton is expected, justifying the observed acceleration of MB photodegradation kinetics.

Marked improvements of the MB photodegradation rates k_{UV-Vis} were further evidenced for all the TiO_2 photonic films after surface functionalization by nanoGO, as shown in Fig. 7(a)–(c). The corresponding enhancement factors were 1.40, 1.45, 1.55 and 1.75 for the PC220, PC350, PC450 and PC510 films, respectively, following closely the increase of nanoGO loading and MB adsorption on the titania walls, a major requirement for the fast electron injection from the dye excited state to the lower lying conduction band of TiO_2 and the efficient self-sensitized dye degradation on titania's surface [70]. In the absence of regeneration, scavenging of the injected TiO_2 conduction band electrons by O_2 molecules lead to the formation of reactive oxygen species (ROS) such as superoxide or hydroperoxide radicals, which in turn may further react to form hydrogen peroxide that produces hydroxyl radicals or even attack on-site the dye molecules, degrading them to non-toxic, harmless end products. To validate such a process, MB degradation experiments were carried out under visible light leading to the kinetics reported in Figs. 7(d) and 6 (f). Likewise UV–vis irradiation experiments, PC425 and nanoGO-PC425 inverse opal films presented the best photocatalytic activity, corroborating the contribution of self-sensitized MB photocatalytic oxidation as the major degradation pathway that becomes synergistically amplified by slow photon effects and the nanoGO-induced adsorption enhancement.

Nevertheless, it is worth noting that optimization of the co-assembly method for the one-step fabrication of TiO_2 inverse opals [71], showed that the corresponding materials are inherently N-doped due to the simultaneous action of TiBALDH as titanium and nitrogen source at an optimum calcination temperature of 400 °C, while GO may also act as broadband photosensitizer of TiO_2 that could contribute to the photocatalytic activity of GO-TiO_2 composites under visible light [30]. Although both effects may promote the visible light photocatalytic performance of nanoGO-PC films beyond self-sensitization, the corresponding photonic enhancements would be expected for the

inverse opals with the lower wavelength stop bands (Table 1), where slow photons may overlap with the spectral regions due to N-doping or even GO sensitization, as shown for N–F co-doped TiO_2 inverse opals [72].

Direct comparison of MB photodegradation for the functionalized GO-PC510 films with the nanoGO-PC510 analogue showed appreciably lower photodegradation rate k_{UV-Vis} (by approximately 33%) (Fig. S9 in Supplementary material). This can be related to both the relatively lower GO coverage of GO-PC510 inferred from Raman spectroscopy (Fig. S6 in Supplementary material) as well as the larger size of the GO sheets that may partially block MB diffusion in the inter-crystalline pores on the inverse opal skeleton walls. The latter was particularly severe in the case of the nanoGO-P25 films, which, despite their high MB adsorptive capacity, presented a modest increase of k_{Vis} [Fig. 7(f)], whereas k_{UV-Vis} even decreased [Fig. 7(c)] compared to the unmodified P25 ones. This detrimental effect can be attributed to the excessive pore clogging of the P25 films by GO nanosheets, in agreement with HR-TEM (Fig. 3), which compromised the diffusion of pollutant molecules through the mesoporous film.

Moreover, the large differences in the initial MB concentrations C_0, especially after nanoGO functionalization, could affect the MB photodegradation kinetics and the corresponding apparent k constants [73]. Assuming that the observed pseudo first-order kinetics of MB degradation arise from Langmuir–Hinshelwood (L-H) model [70,74], the initial reaction rate r becomes proportional to C_0 at low (< mM) MB concentrations, $r = k_{app}C_0$. Fig. 8 compares the corresponding reaction rates r_{UV-Vis} and r_{Vis} for all the pristine and nanoGO functionalized films under UV–vis and visible light. Significant enhancement of r_{UV-Vis} was invariably observed for all films, most prominent for nanoGO-PC510, apart from nanoGO-P25 due to the excessive pore blockage, validating the beneficial effect of nanoGO surface modification in the inverse opal structure. The improvement of the reaction rates was moderated in the case of r_{Vis}, indicating that the observed increase of the apparent k_{Vis} under visible light originated mainly from the enhanced MB adsorption on the nanocrystalline TiO_2 skeleton. Nevertheless, to validate these effects rigorous kinetic models should be developed in order to take into account possible external and internal mass transfer limitations [75]
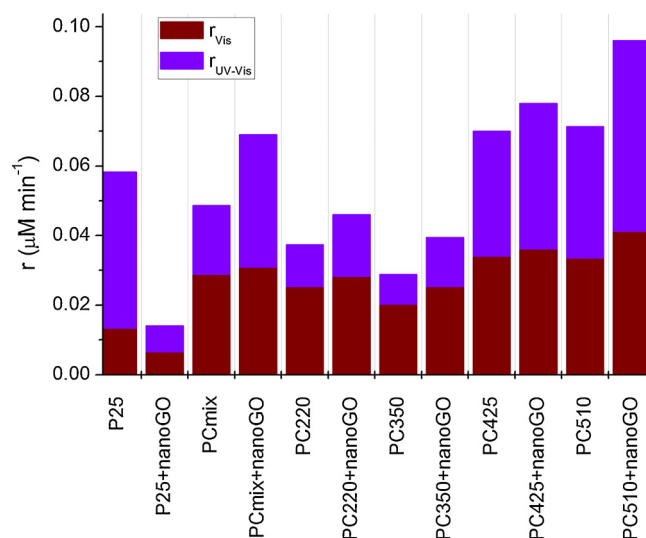
Fig. 8. Reaction rates $r_{UV–vis}$ and r_{Vis} under UV–vis and visible light illumination for the pristine and nanoGO functionalized inverse opal and reference films.

due to the confined pollutant diffusion in the immobilized macro/mesoporous periodic catalysts [43,44]. In addition, advanced kinetic modeling including the effect of photon absorption by the inverse opal catalyst should be applied in order to delineate the intrinsic reaction rates [76,77].

Furthermore, it should be noted that pristine and functionalized PCmix reference films presented considerable photocatalytic activity under both UV–vis and visible light irradiation (Fig. 7).This indicates that despite the suppression of photonic effects due to lattice disorder, the macro-mesoporous structure of PCmix appreciably increases reactivity by enhancing adsorption and molecular diffusion and possibly light harvesting via multiple scattering, all being key aspects in aqueous phase photocatalysis, where slow photon effects are inevitably moderated due to the reduced refractive index contrast of TiO_2 with water [78]. Consecutive MB photodegradation tests for the functionalized nanoGO-PC510 corroborated the excellent stability of the films, while SEM, UV–vis and Raman measurements after the MB degradation confirmed that the film retained intact its photonic properties and nanoGO loading (Fig. S10 in Supplementary material).

3.3. Adsorption and electron transfer in nanoGO-TiO$_2$ PCs

The identification of slow photon effects in relation to the pollutant adsorption was further explored by Raman spectroscopy at excitation wavelengths of 514 and 785 nm using dye sensitized photonic films in 0.1 mM MB aqueous solution. Fig. 9(a) and (b) displays the Raman spectra of the MB sensitized inverse opals, before and after nanoGO deposition, at 514 nm. Comparison to the Raman spectrum of pure MB powder allowed discriminating the dye Raman bands from the anatase TiO_2 ones, whose relative intensity was quantified by the intensity ratio I_{MB}/I_{TiO2} of the strongest C–C ring stretching vibration (1628 cm^{-1}) of the adsorbed MB molecules to the intense anatase E_g mode (148 cm^{-1}) serving as internal reference. A marked increase of the I_{MB}/I_{TiO2} ratio was accordingly detected upon nanoGO loading, reflecting the enhanced MB adsorption on the functionalized nanocrystalline inverse opal walls, as shown in Fig. 7(d). However, the relative intensity ratio presented a non-monotonous macropore size dependence with a pronounced enhancement/decline for both pristine and nanoGO-functionalized PC350/PC425 photonic films, respectively, in apparent contrast to the dark MB adsorption results [Fig. 7(d)], where the opposite behavior was observed (the PC350/PC425 films presented the minimum/maximum MB uptake). This variation is a direct manifestation of

photonic effects, where the incident 514 nm laser excitation falls within the broad, red slow photon region of PC350, leading to the enhanced scattering of the laser beam along with the intense DR% within the TiO_2 skeleton [Fig. 5(c)]. This results in a strong increase of the Raman signal from the adsorbed MB molecules on the TiO_2 inverse opal walls despite the low dye loading, an effect that can be ideally applied for the development of noble metal-free surface enhanced Raman spectroscopy (SERS) substrates for organics detection and reaction monitoring [59,79]. The reverse effect occurred for the PC425 films, where the 514 nm excitation approached closely the film's stop band at 530 nm [Table 1, and Fig. 5(b)] leading to the Bragg reflection of the laser beam and the attenuation of the MB Raman signal, regardless of the extended dye adsorption. To attest this slow photon scattering enhancement, additional Raman measurements were carried out at 785 nm laser excitation [Fig. 9(c)], which was far above the air stop bands of most photonic films (Table 1). In that case, though, appreciable MB Raman signal could be only detected for the nanoGO-PC films, in contrast to the 514 nm Raman spectra. This can be mainly related to the weak but finite MB electronic absorption at 514 nm that enhances the MB Raman cross section, in contrast to the NIR (785 nm) excitation were no MB absorption can be traced (Fig. S11 in Supplementary material). At 785 nm, the I_{MB}/I_{TiO2} ratio was minimized for nanoGO-PC350, as shown in Fig. 9(c) and (d), reflecting its lowest MB adsorption capacity determined from dark adsorption [Fig. 7(d)]. On the other hand, the strongly dye adsorbing nanoGO-PC425 presented considerably higher I_{MB}/I_{TiO2} values, while nanoGO-PC510 showed the maximum intensity ratio. The latter, however, may have been increased to some extent as the laser wavelength approaches the extended red slow photon region, inferred from the broad DR% spectra of PC510 [Fig. 5(a)] [80].

Besides its unique adsorption capacity, nanoGO sheets may further contribute to the photocatalytic activity by means of interfacial electron transfer and transport. This was investigated using light induced EPR spectroscopy at low temperatures. Fig. 10 compares the EPR spectra of the most efficient PC425 and nanoGO-PC425 inverse opals before and after UVA and white light illumination at 12 K. Under dark conditions, no appreciable EPR signal could be detected for the pristine PC425 besides a weak narrow EPR line at $g = 2.003$ possibly due to trapped electrons on oxygen vacancies [81]. Upon UVA illumination, an anisotropic EPR signal emerged at $g > 2.00$ that after subtraction of the corresponding "dark" spectrum resembled an unresolved axial-like powder spectrum with $g_\perp \approx 2.014$ and $g_{||} \approx 2.0044$ [Fig. 10(a)], which is characteristic of photogenerated oxygen radicals such as O$^-$ arising from trapped holes at O^{2-} ions [82].

On the other hand, white light illumination resulted in the appearance of a broad EPR powder spectrum of rhombic-like symmetry with g-values of $g_x \approx 2.003$, $g_y \approx 2.009$ and $g_z \approx 2.030$ [Fig. 10(c)], where the main contribution arises from superoxide anions (O$_2{}^-$) [83]. Moreover, no EPR signal was observed at $g < 2.00$, where the EPR spectra of localized Ti^{3+} ions originating from trapped electrons at lattice or surface Ti^{4+} sites are expected, implying that most of the photogenerated electrons become scavenged by adsorbed O_2 and/or remain delocalized in the conduction band, similar to anatase nanoparticles calcined at T < 550 °C [84].

In the case of nanoGO-PC425 [Fig. 10(b) and (d)], the typical sextet hyperfine pattern of dilute Mn^{2+} ($S = 5/2$, $I = 5/2$) ions originating from residuals of potassium permanganate in the GO synthesis [85] was observed along with a narrow resonance line at $g = 2.0028$, characteristic of localized defect spins in GO [86]. Illumination of nanoGO-PC425 resulted, after subtraction of the dark spectra, in the appearance of a narrow, slightly asymmetric EPR line at $g \approx 2.0040$, most prominent for UVA light. The g-factor and narrow width of this EPR line suggest the light-induced formation of an unpaired spin radical in nanoGO that could be generated via the scavenging of the UVA excited electrons in TiO_2.

This was further supported by direct PL spectroscopy on the PC425 and nanoGO-PC425 inverse opals, as shown in Fig. 11. The PL spectra
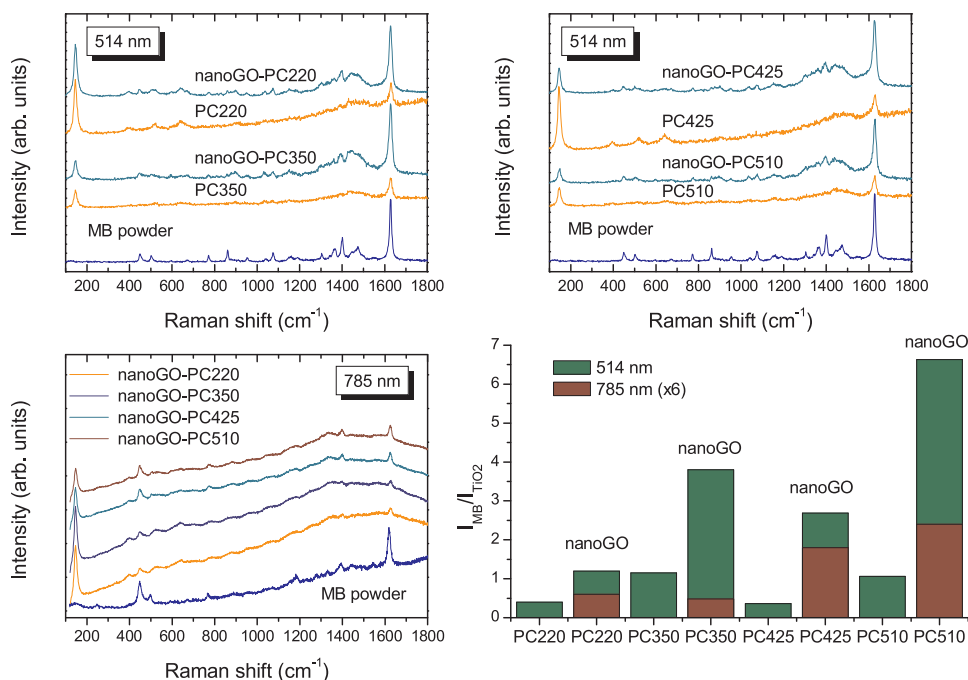
Fig. 9. Raman spectra of the MB (0.1 mM) sensitized TiO$_2$ inverse opals, before and after nanoGO deposition, at (a)–(b) 514 and (c) 785 nm. (d) Macropore size dependence of the I_{MB}/I_{TiO2} intensity ratio at 514 and 785 nm excitation wavelengths.

of the unmodified film revealed a broad emission peak at 395 nm along with a weaker shoulder at 374 nm, which can be attributed to the band-to-band phonon-assisted indirect transitions of anatase [87,88], close to its absorption edge at 375 nm (Fig. 5). Surface deposition of nanoGO resulted in a drastic reduction of the PL intensity, corroborating the interfacial transfer of UV photogenerated electrons from the anatase nanocrystallites to the GO nanosheets. We may accordingly conclude that nanoGO deposition increased further pollutant degradation by
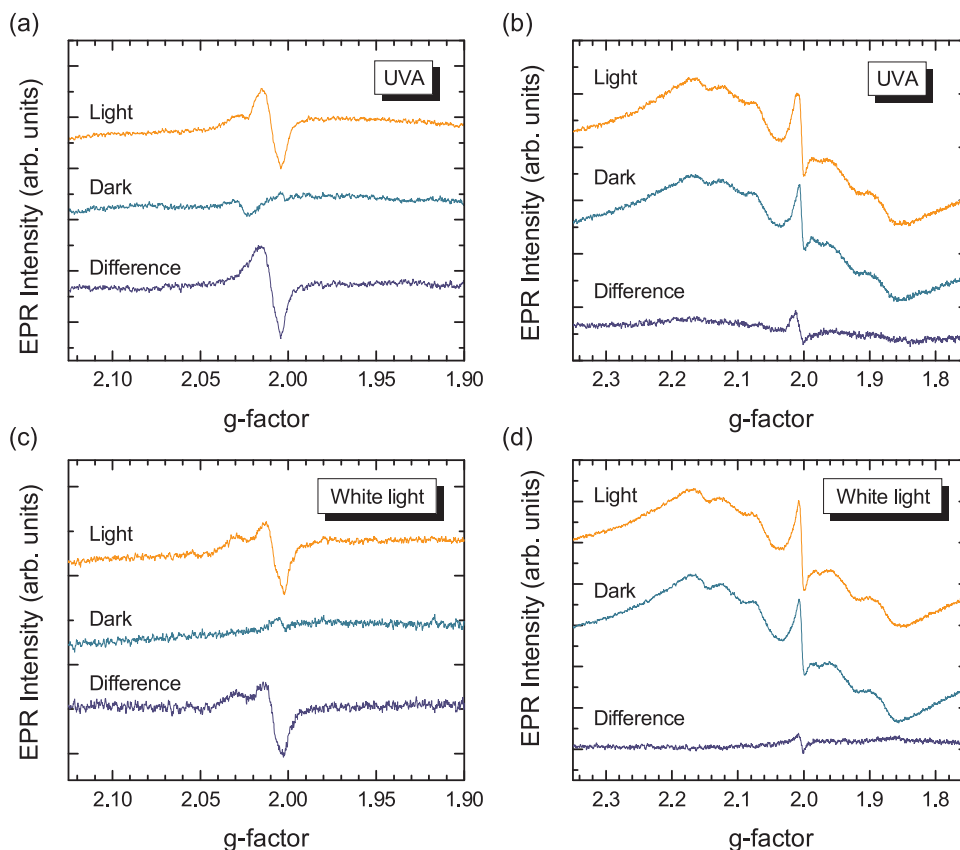
Fig. 10. EPR spectra of PC425 (a), (c) and nanoGO-PC425 (b), (d) inverse opals under dark and UVA (a), (b) and white light (c), (d) illumination and the corresponding difference spectra at 12 K.
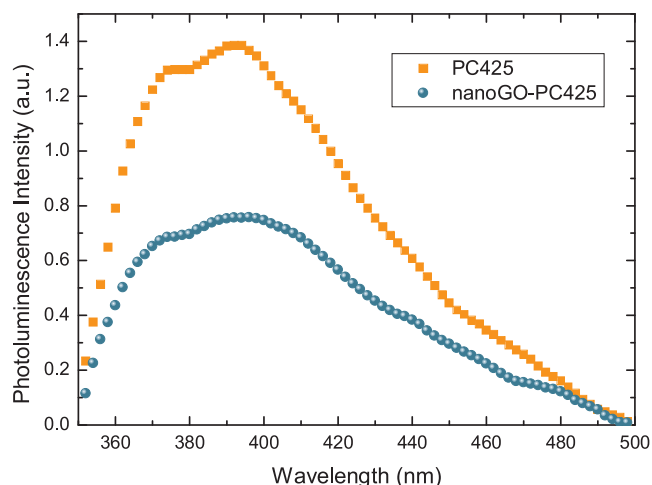
Fig. 11. PL spectra of PC425 and nanoGO-PC425.

enhancing charge separation under UV–vis irradiation, independently of dye adsorption, complying with the increase of the corresponding reaction rates r_{UV-vis} (Fig. 8).

Fig. 12 presents a tentative charge transfer and reaction scheme of individual TiO$_2$ crystallites in the nanoGO-PC films. Photogenerated electrons in TiO$_2$ by UV light as well as electrons excited in the adsorbed (by electrostatic and π-π interactions) MB molecules by visible light are scavenged and shuttled in the GO nanosheets covering the titania nanoparticles on the inverse opal skeleton. The MB molecules may then be degraded by hydroxyl radicals formed directly by valence band holes of TiO$_2$ or via intermediate peroxide or other radicals formed in the GO sheets [73,74]. Based on both EPR and PL results, GO is inferred to act as an electron sink, similar to most GO-TiO$_2$ composites [89], because of its higher work function than the conduction band edge of TiO$_2$ [90,91].

4. Conclusions

Photonic band gap engineered TiO$_2$ inverse opal films were fabricated by the convective evaporation-induced co-assembly of polystyrene colloidal spheres with the water soluble TiBALDH precursor leading to well-ordered nanocrystalline photonic films with controlled structural and optical properties. Surface functionalization was performed by GO nanocolloids at loadings determined by the macropore size with minimal effects on the inverse opal long range order and photonic properties according to scanning and transmission electron microscopy, specular and diffuse UV–vis reflectance, Raman spectroscopy and N$_2$ porosimetry. Although the mesoporosity of the nanocrystalline titania walls was reduced by the GO nanosheet deposition, their surface functionality was significantly improved by the abundant oxygen groups leading to enhanced pollutant adsorption. Slow photon amplification in the aqueous phase MB photodegradation was identified for the pristine TiO$_2$ photonic films under both UV–vis and Vis light, when the low energy edge of the inverse opal stop band (in water) approached the MB electronic absorption at 664 nm, enabling slow light propagation of (red) photons localized in the titania skeleton within the MB electronic absorption spectral range that accelerated the dye photodegradation kinetics. Marked improvements of the MB photodegradation under UV–vis and Vis light were further evinced on the functionalized TiO$_2$ inverse opals, depending on the amount of nanoGO loading and the concomitant MB adsorption on the TiO$_2$ walls, a major requirement for the self-sensitized dye photocatalysis. Specifically, TiO$_2$ photonic films with the higher void diameters and nanoGO loadings presented the highest degradation rates because of the combination of slow photon effects, adsorption and interfacial charge transfer. In fact, light induced spin radicals identified by EPR spectroscopy and PL quenching indicated that GO nanosheets act as scavengers of UV-generated electrons in TiO$_2$, assisting further MB degradation under UV–vis light. Comparative photocatalytic tests using functionalized inverse opal films in regular, micrometer-sized GO sheets showed lower photocatalytic activity corroborating the unique functionality and adsorption capacity of nanoGO due to its high surface charge density. On the other hand, nanoGO deposition on benchmark mesoporous P25 films resulted in reduction of their high photocatalytic activity on MB degradation, especially under UV–vis light, due to the excessive mesopore clogging by the GO nanosheets that obstructed easy diffusion of pollutant molecules during aqueous phase photocatalysis. Lower though considerable photocatalytic activity was also observed for disordered photonic films, indicating that the macro-mesoporous inverse opal structure even in the absence of long range periodicity and photonic enhancement effects, may appreciably promote the photocatalytic reactivity by improving adsorption, molecular diffusion and light harvesting via multiple scattering. Synergy of the unique potential of macro-mesoporous TiO$_2$ inverse opals for enhanced slow light trapping
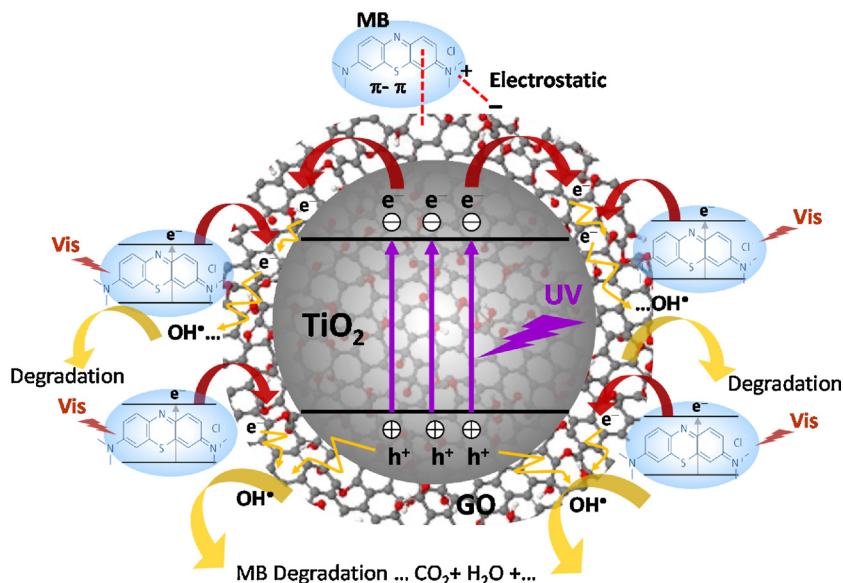

Fig. 12. Schematic of MB adsorption, interfacial electron transfer and reaction of nanoGO-TiO$_2$ photonic films.

and mass transport with the improved adsorption capacity and charge separation of nanoGO is essential for the development of highly efficient thin film photocatalysts.

Acknowledgments

Appendix A. Supplementary data

Supplementary material related to this article can be found, in the online version, at doi:https://doi.org/10.1016/j.apcatb.2018.08.080.

References

[1] A. Fujishima, X. Zhang, D.A. Tryk, TiO$_2$ photocatalysis and related surface phenomena, Surf. Sci. Rep. 63 (2008) 515–582.

[2] J. Schneider, D. Bahnemann, J. Ye, G. Li Puma, D.D. Dionysiou (Eds.), Photocatalysis: Fundamentals and Perspectives, RSC Energy and Environment Series No. 14, The Royal Society of Chemistry, 2016.

[3] Y. Ma, X. Wang, Y. Jia, X. Chen, H. Han, C. Li, Titanium dioxide-based nanomaterials for photocatalytic fuel generations, Chem. Rev. 114 (2014) 9987–10043.

[4] P. Lianos, Review of recent trends in photoelectrocatalytic conversion of solar energy to electricity and hydrogen, Appl. Catal. B: Environ. 210 (2017) 235–254.

[5] S. Loeb, R. Hofmann, J.-H. Kim, Beyond the Pipeline: assessing the efficiency limits of advanced technologies for solar water disinfection, Environ. Sci. Technol. Lett. 3 (2016) 73–80.

[6] A.V. Emeline, X. Zhang, M. Jin, T. Murakami, A. Fujishima, Application of a "black body" like reactor for measurements of quantum yields of photochemical reactions in heterogeneous systems, J. Phys. Chem. B 110 (2006) 7409–7413.

[7] B. Liu, X. Zhao, C. Terashima, A. Fujishima, K. Nakata, Thermodynamic and kinetic analysis of heterogeneous photocatalysis for semiconductor systems, Phys. Chem. Chem. Phys. 16 (2014) 8751–8760.

[8] M. Pelaez, N.T. Nolan, S.C. Pillai, M.K. Seery, P. Falaras, A.G. Kontos, P.S.M. Dunlop, J.W.J. Hamilton, J.A. Byrne, K. O'Shea, M.H. Entezari, D.D. Dionysiou, A review on the visible light active titanium dioxide photocatalysts for environmental applications, Appl. Catal. B: Environ. 125 (2012) 331–349.

[9] J.I.L. Chen, G. von Freymann, S.Y. Choi, V. Kitaev, G.A. Ozin, Amplified photochemistry with slow photons, Adv. Mater. 18 (2006) 1915–1919.

[10] E. Armstrong, C. O'Dwyer, Artificial opal photonic crystals and inverse opal structures–fundamentals and applications from optics to energy storage, J. Mater. Chem. C 3 (2015) 6109–6143.

[11] M. Curti, J. Schneider, D.W. Bahnemann, C.B. Mendive, Inverse opal photonic crystals as a strategy to improve photocatalysis: underexplored questions, J. Phys. Chem. Lett. 6 (2015) 3903–3910.

[12] J.J. Pietron, P.A. DeSario, Review of roles for photonic crystals in solar fuels photocatalysis, J. Photon. Energy 7 (2016) 012007.

[13] J. Liu, H. Zhao, M. Wu, B. Van der Schueren, Y. Li, O. Deparis, J. Ye, G.A. Ozin, T. Hasan, B.-L. Su, Slow photons for photocatalysis and photovoltaics, Adv. Mater. 29 (2017) 1605349.

[14] V. Likodimos, Photonic crystal-assisted visible light activated TiO$_2$ photocatalysis, Appl. Catal. B: Environ. 230 (2018) 269–303.

[15] A. Stein, B.E. Wilson, S.G. Rudisill, Design and functionality of colloidal-crystal-templated materials-chemical applications of inverse opals, Chem. Soc. Rev. 42 (2013) 2763–2803.

[16] N. Vogel, M. Retsch, C.-A. Fustin, A. del Campo, U. Jonas, Advances in colloidal assembly: the design of structure and hierarchy in two and three dimensions, Chem. Rev. 115 (2015) 6265–6311.

[17] K.R. Phillips, G.T. England, S. Sunny, E. Shirman, T. Shirman, N. Vogel, J. Aizenberg, A colloidoscope of colloid-based porous materials and their uses, Chem. Soc. Rev. 45 (2016) 281–322.

[18] X. Li, J. Yu, M. Jaroniec, Hierarchical photocatalysts, Chem. Soc. Rev. 45 (2016) 2603–2636.

[19] X.-Y. Yang, L.-H. Chen, Y. Li, J.C. Rooke, C. Sanchez, B.-L. Su, Hierarchically porous materials: synthesis strategies and structure design, Chem. Soc. Rev. 46 (2017) 481–558.

[20] S. Banerjee, S.C. Pillai, P. Falaras, K.E. O'Shea, J.A. Byrne, D.D. Dionysiou, New insights into the mechanism of visible light photocatalysis, J. Phys. Chem. Lett. 5 (2014) 2543–2554.

[21] R. Asahi, T. Morikawa, H. Irie, T. Ohwaki, Nitrogen-doped titanium dioxide as visible-light-sensitive photocatalyst: designs, developments, and prospects, Chem. Rev. 114 (2014) 9824–9852.

[22] C. Clavero, Plasmon-induced hot-electron generation at nanoparticle/metal-oxide interfaces for photovoltaic and photocatalytic devices, Nat. Photon. 8 (2014) 95–103.

[23] X. Meng, L. Liu, S. Ouyang, H. Xu, D. Wang, N. Zhao, J. Ye, Nanometals for solar-to-chemical energy conversion: from semiconductor-based photocatalysis to plasmon-mediated photocatalysis and photo-thermocatalysis, Adv. Mater. 28 (2016) 6781–6803.

[24] H. Tada, Q. Jin, A. Iwaszuk, M. Nolan, Molecular-scale transition metal oxide nanocluster surface-modified titanium dioxide as solar-activated environmental catalysts, J. Phys. Chem. C 118 (2014) 12077–12086.

[25] W.G. Tu, Y. Zhou, Z.G. Zou, Versatile graphene promoting photocatalytic performance of semiconductors: basic principles, synthesis, solar energy conversion, and environmental applications, Adv. Funct. Mater. 23 (2013) 4996–5008.

[26] S.M. Miranda, G.E. Romanos, V. Likodimos, R.R.N. Marques, E.P. Favvas, F.K. Katsaros, K.L. Stefanopoulos, V.J.P. Vilar, J.L. Faria, P. Falaras, A.M.T. Silva, Pore structure, interface properties and photocatalytic efficiency of hydration/dehydration derived TiO$_2$/CNT composites, Appl. Catal. B: Environ. 147 (2014) 65–81.

[27] X. Gong, G. Liu, Y. Li, D.Y.W. Yu, W.Y. Teoh, Functionalized-graphene composites: fabrication and applications in sustainable energy and environment, Chem. Mater. 28 (2016) 8082–8118.

[28] S. Dervin, D.D. Dionysiou, S.C. Pillai, 2D nanostructures for water purification: graphene and beyond, Nanoscale 8 (2016) 15115–15131.

[29] L.M. Pastrana-Martínez, S. Morales-Torres, V. Likodimos, P. Falaras, J.L. Figueiredo, J.L. Faria, A.M.T. Silva, Role of oxygen functionalities on the synthesis of photocatalytically active graphene-TiO$_2$ composites, Appl. Catal. B: Environ. 158–159 (2014) 329–340.

[30] N. Zhang, M.-Q. Yang, S. Liu, Y. Sun, Y.-J. Xu, Waltzing with the versatile platform of graphene to synthesize composite photocatalysts, Chem. Rev. 115 (2015) 10307–10377.

[31] A. Morais, C. Longo, J.R. Araujo, M. Barroso, J.R. Durrant, A.F. Nogueira, Nanocrystalline anatase TiO$_2$/reduced graphene oxide composite films as photoanodes for photoelectrochemical water splitting studies: the role of reduced graphene oxide, Phys. Chem. Chem. Phys. 18 (2016) 2608–2616.

[32] J. Du, X. Lai, N. Yang, J. Zhai, D. Kisailus, F. Su, D. Wang, L. Jiang, Hierarchically ordered macro-mesoporous TiO$_2$–graphene composite films: improved mass transfer, reduced charge recombination, and their enhanced photocatalytic activities, ACS Nano 5 (2011) 590–596.

[33] R. Boppella, S.T. Kochuveedu, H. Kim, M.J. Jeong, F.M. Mota, J.H. Park, D.H. Kim, Plasmon-sensitized graphene/TiO$_2$ inverse opal nanostructures with enhanced charge collection efficiency for water splitting, ACS Appl. Mater. Interfaces 9 (2017) 7075–7083.

[34] S. Lee, Y. Lee, D.H. Kim, J.H. Moon, Carbon-deposited TiO$_2$ 3D inverse opal photocatalysts: visible-light photocatalytic activity and enhanced activity in a viscous solution, ACS Appl. Mater. Interfaces 5 (2013) 12526–12532.

[35] J. Luo, L.J. Cote, V.C. Tung, A.T.L. Tan, P.E. Goins, J. Wu, J. Huang, Graphene oxide nanocolloids, J. Am. Chem. Soc. 132 (2010) 17667–17669.

[36] H.-I. Kim, G.-H. Moon, D. Monllor-Satoca, Y. Park, W. Choi, Solar photoconversion using graphene/TiO$_2$ composites: nanographene shell on TiO$_2$ core versus TiO$_2$ nanoparticles on graphene sheet, J. Phys. Chem. C 116 (2012) 1535–1543.

[37] C. Zhu, P. Liu, A.P. Mathew, Self-assembled TEMPO cellulose nanofibers: graphene oxide-based biohybrids for water purification, ACS Appl. Mater. Interfaces 9 (2017) 21048–21058.

[38] B. Hatton, L. Mishchenko, S. Davis, K.H. Sandhage, J. Aizenberg, Assembly of large-area, highly ordered, crack-free inverse opal films, PNAS 107 (2010) 10354–10359.

[39] Z. Cai, Z. Xiong, X. Lu, J. Teng, In situ gold-loaded titania photonic crystals with enhanced photocatalytic activity, J. Mater. Chem. A 2 (2014) 545–553.

[40] T. Tsoufis, F. Katsaros, Z. Sideratou, G. Romanos, O. Ivashenko, P. Rudolf, B.J. Kooi, S. Papageorgiou, M.A. Karakassides, Tailor-made graphite oxide–DAB poly(propylene imine) dendrimer intercalated hybrids and their potential for efficient CO$_2$ adsorption, Chem. Commun. 50 (2014) 10967–10970.

[41] T. Tsoufis, F. Katsaros, Z. Sideratou, B.J. Kooi, M.A. Karakassides, A. Siozios, Intercalation study of low-molecular-weight hyperbranched polyethyleneimine into graphite oxide, Chem. Eur. J. 20 (2014) 8129–8137.

[42] M. Zhou, J. Bao, Y. Xu, J.J. Zhang, J.F. Xie, M.L. Guan, C.L. Wang, L.Y. Web, Y. Lei, Y. Xie, Photoelectrodes based upon Mo:BiVO$_4$ inverse opals for photoelectrochemical water splitting, ACS Nano 8 (2014) 7088–7098.

[43] T. Cherdhirankorn, M. Retsch, U. Jonas, H.-J. Butt, K. Koynov, Tracer diffusion in silica inverse opals, Langmuir 26 (2010) 10141–10146.

[44] R. Raccis, A. Nikoubashman, M. Retsch, U. Jonas, K. Koynov, H.-J. Butt, C.N. Likos, G. Fytas, Confined diffusion in periodic porous nanostructures, ACS Nano 5 (2011) 4607–4616.

[45] K.R. Phillips, T. Shirman, E. Shirman, A.V. Shneidman, T.M. Kay, J. Aizenberg, Nanocrystalline precursors for the co-assembly of crack-free metal oxide inverse opals, Adv. Mater. 30 (2018) 1706329.

[46] U. Balachandran, N.G. Eror, Raman spectra of titanium dioxide, J. Solid State Chem. 42 (1982) 276–282.

[47] V. Likodimos, T. Stergiopoulos, P. Falaras, R. Harikisun, J. Desilvestro, G. Tulloch, Prolonged light and thermal stress effects on industrial dye-sensitized solar cells: a micro-Raman investigation on the long-term stability of aged cells, J. Phys. Chem. C 113 (2009) 9412–9422.

[48] S. Kelly, F.H. Pollak, M. Tomkiewicz, Raman spectroscopy as a morphological probe for TiO$_2$ aerogels, J. Phys. Chem. B 101 (1997) 2730–2734.

[49] S. Balaji, Y. Djaoued, J. Robichaud, Phonon confinement studies in nanocrystalline anatase-TiO$_2$ thin films by micro Raman spectroscopy, J. Raman Spectrosc. 37 (2006) 1416–1422.

[50] V. Likodimos, T. Stergiopoulos, P. Falaras, J. Kunze, P. Schmuki, Phase composition, size, orientation, and antenna effects of self-assembled anodized titania nanotube arrays: a polarized micro-Raman investigation, J. Phys. Chem. C 112 (2008) 12687–12696.

[51] H. Möckel, M. Giersig, F. Willig, Formation of uniform size anatase nanocrystals from bis(ammonium lactato)titanium dihydroxide by thermohydrolysis, J. Mater. Chem. 9 (1999) 3051–3056.

[52] K. Pelentridou, E. Stathatos, P. Lianos, V. Drakopoulos, A new precursor for the preparation of nanocrystalline TiO_2 films and their photocatalytic properties, J. Nanosci. Nanotechnol. 10 (2010) 6093–6098.

[53] A.-L. Anderson, R. Binions, A preferential precursor for photocatalytically active titanium dioxide thin films: titanium bis-ammonium lactato dihydroxide as an alternative to titanium tetra iso-propoxide, Polyhedron 118 (2016) 81–90.

[54] G.A. Seisenbaeva, G. Daniel, J.-M. Nedelecde, V.G. Kessler, Solution equilibrium behind the room-temperature synthesis of nanocrystalline titanium dioxide, Nanoscale 5 (2013) 3330–3336.

[55] M. Wu, J. Jin, J. Liu, Z. Deng, Y. Li, O. Deparis, B.-L. Su, High photocatalytic activity enhancement of titania inverse opal films by slow photon effect induced strong light absorption, J. Mater. Chem. A 1 (2013) 15491–15500.

[56] M. Wu, J. Liu, J. Jin, C. Wang, S. Huang, Z. Deng, Y. Li, B.-L. Su, Probing significant light absorption enhancement of titania inverse opal films for highly exalted photocatalytic degradation of dye pollutants, Appl. Catal. B: Environ. 150–151 (2014) 411–420.

[57] D. Qi, L. Lu, Z. Xi, L. Wang, J. Zhang, Enhanced photocatalytic performance of TiO_2 based on synergistic effect of Ti^{3+} self-doping and slow light effect, Appl. Catal. B: Environ. 160–161 (2014) 621–628.

[58] K.N. Kudin, B. Ozbas, H.C. Schniepp, R.K. Prud'homme, I.A. Aksay, R. Car, Raman spectra of graphite oxide and functionalized graphene sheets, Nano Lett. 8 (2007) 36–41.

[59] D. Qi, L. Lu, L. Wang, J. Zhang, Improved SERS sensitivity on plasmon-free TiO_2 photonic microarray by enhancing light-matter coupling, J. Am. Chem. Soc. 136 (2014) 9886–9889.

[60] L.M. Pastrana-Martínez, S. Morales-Torres, V. Likodimos, J.L. Figueiredo, J.L. Faria, P. Falaras, A.M.T. Silva, Advanced nanostructured photocatalysts based on reduced graphene oxide–TiO_2 composites for degradation of diphenhydramine pharmaceutical and methyl orange dye, Appl. Catal., B: Environ. 123–124 (2012) 241–256.

[61] R.C. Schroden, M. Al-Daous, C.F. Blanford, A. Stein, Optical properties of inverse opal photonic crystals, Chem. Mater. 14 (2002) 3305–3315.

[62] V. Jovic, H. Idriss, G.I.N. Waterhouse, Slow photon amplification of gas-phase ethanol photo-oxidation in titania inverse opal photonic crystals, Chem. Phys. 479 (2016) 109–121.

[63] V. Yannopapas, N. Stefanou, A. Modinos, Effect of stacking faults on the optical properties of inverted opals, Phys. Rev. Lett. 86 (2001) 4811–4814.

[64] V.N. Astratov, A.M. Adawi, S. Fricker, M.S. Skolnick, D.M. Whittaker, P.N. Pusey, Interplay of order and disorder in the optical properties of opal photonic crystals, Phys. Rev. B 66 (2002) 165215.

[65] J.F. Galisteo-López, M. Galli, M. Patrini, A. Balestreri, L.C. Andreani, C. López, Effective refractive index and group velocity determination of three-dimensional photonic crystals by means of white light interferometry, Phys. Rev. B 73 (2006) 125103.

[66] J.S. King, E. Graugnard, C.J. Summers, TiO_2 inverse opals fabricated using low-temperature atomic layer deposition, Adv. Mater. 17 (2005) 1010–1013.

[67] X. Zheng, S. Meng, J. Chen, J. Wang, J. Xian, Y. Shao, X. Fu, D. Li, Titanium dioxide photonic crystals with enhanced photocatalytic activity: matching photonic band gaps of TiO_2 to the absorption peaks of dyes, J. Phys. Chem. C 117 (2013) 21263–21273.

[68] H. Kim, S.-O. Kang, S. Park, H.S. Park, Adsorption isotherms and kinetics of cationic and anionic dyes on three-dimensional reduced graphene oxide macrostructure, J. Ind. Eng. Chem. 21 (2015) 1191–1196.

[69] S. Meng, D. Li, P. Wang, X. Zheng, J. Wang, J. Chen, J. Fang, X. Fu, Probing photonic effect on photocatalytic degradation of dyes based on 3D inverse opal ZnO photonic crystal, RSC Adv. 3 (2013) 17021–17028.

[70] I.K. Konstantinou, T.A. Albanis, TiO_2-assisted photocatalytic degradation of azo dyes in aqueous solution: kinetic and mechanistic investigations: a review, Appl. Catal. B: Environ. 49 (2004) 1–14.

[71] Z.Y. Hu, L.B. Xu, L.L. Wang, Y. Huang, L.M. Xu, J.F. Chen, One-step fabrication of N-doped TiO_2 inverse opal films with visible light photocatalytic activity, Catal. Commun. 40 (2013) 106–110.

[72] T.K. Rahul, N. Sandhyarani, Nitrogen-fluorine co-doped titania inverse opals for enhanced solar light driven photocatalysis, Nanoscale 7 (2015) 18259–18270.

[73] T. Zhang, T. Oyama, A. Aoshima, H. Hidaka, J. Zhao, N. Serpone, Photooxidative N-demethylation of methylene blue in aqueous TiO_2 dispersions under UV irradiation, J. Photochem. Photobiol. A Chem. 140 (2001) 163–172.

[74] A. Houas, H. Lachheb, M. Ksibi, E. Elaloui, C. Guillard, J.M. Hermann, Photocatalytic degradation pathway of methylene blue in water, Appl. Catal. B: Environ. 31 (2001) 145–157.

[75] D. Chen, F. Li, A.K. Ray, External and internal mass transfer effect on photocatalytic degradation, Catal. Today 66 (2001) 475–485.

[76] M.J. Muñoz-Batista, M.M. Ballari, A.E. Cassano, O.M. Alfano, A. Kubacka, M. Fernández-García, Ceria promotion of acetaldehyde photo-oxidation in a TiO_2-based catalyst: a spectroscopic and kinetic study, Catal. Sci. Technol. 5 (2015) 1521–1531.

[77] A. Manassero, M.L. Satuf, O.M. Alfano, Kinetic modeling of the photocatalytic degradation of clofibric acid in a slurry reactor, Environ. Sci. Pollut. Res. 22 (2015) 926–937.

[78] J.I.L. Chen, G.A. Ozin, Heterogeneous photocatalysis with inverse titania opals: probing structural and photonic effects, J. Mater. Chem. 19 (2009) 2675–2678.

[79] A. Toumazatou, M.K. Arfanis, P.-A. Pantazopoulos, A.G. Kontos, P. Falaras, N. Stefanou, V. Likodimos, Slow-photon enhancement of dye sensitized TiO_2 photocatalysis, Mater. Lett. 197 (2017) 123–126.

[80] D. Qi, X. Yan, L. Wang, J. Zhang, Plasmon-free SERS self-monitoring of catalysis reaction on Au nanoclusters/TiO_2 photonic microarray, Chem. Commun. 51 (2015) 8813–8816.

[81] I. Nakamura, N. Negishi, S. Kutsuna, T. Ihara, S. Sugihara, K. Takeuchi, Role of oxygen vacancy in the plasma-treated TiO_2 photocatalyst with visible light activity for NO removal, J. Mol. Catal. A Chem. 161 (2000) 205–212.

[82] T. Berger, M. Sterrer, O. Diwald, E. Knözinger, D. Panayotov, T.L. Thompson, J.T. Yates Jr, Light-induced charge separation in anatase TiO_2 particles, J. Phys. Chem. B 109 (2005) 6061–6068.

[83] E. Carter, A.F. Carley, D.M. Murphy, Evidence for O_2- radical stabilization at surface oxygen vacancies on polycrystalline TiO_2, J. Phys. Chem. C 111 (2007) 10630–10638.

[84] V. Likodimos, A. Chrysi, M. Calamiotou, C. Fernández-Rodríguez, J.M. Doña-Rodríguez, D.D. Dionysiou, P. Falaras, Microstructure and charge trapping assessment in highly reactive mixed phase TiO_2 photocatalysts, Appl. Catal. B: Environ. 192 (2016) 242–252.

[85] A.M. Panich, A.I. Shames, N.A. Sergeev, Paramagnetic impurities in graphene oxide, Appl. Magn. Reson. 44 (2013) 107–116.

[86] A. Diamantopoulou, S. Glenis, G. Zolnierkiwicz, N. Guskos, V. Likodimos, Magnetism in pristine and chemically reduced graphene oxide, J. Appl. Phys. 121 (2017) 043906.

[87] N. Serpone, D. Lawless, R. Khairutdinov, Size effects on the photophysical properties of colloidal anatase TiO_2 particles: size quantization versus direct transitions in this indirect semiconductor? J. Phys. Chem. 99 (1995) 16646–16654.

[88] L. Kernazhitsky, V. Shymanovska, T. Gavrilko, V. Naumov, L. Fedorenko, V. Kshnyakin, J. Baran, Room temperature photoluminescence of anatase and rutile TiO_2 powders, J. Lumin. 146 (2014) 199–204.

[89] R. Giovannetti, E. Rommozzi, M. Zannotti, C.A. D'Amato, Recent advances in graphene based TiO_2 nanocomposites ($GTiO_2Ns$) for photocatalytic degradation of synthetic dyes, Catalysts 7 (2017) 305 (34).

[90] P.V. Kumar, M. Bernardi, J.C. Grossman, The impact of functionalization on the stability, work function, and photoluminescence of reduced graphene oxide, ACS Nano 7 (2013) 1638–1645.

[91] T.F. Yeh, J. Cihlar, C.Y. Chang, C. Cheng, H.S. Teng, Roles of graphene oxide in photocatalytic water splitting, Mater. Today 16 (2013) 78–84.